Zircon U–Pb geochronology, major-trace elements and Sr–Nd isotope geochemistry of Mashhad granodiorites (NE Iran) and their mafic microgranular enclaves: evidence for magma mixing and mingling

Maryam Deyhimi, Ali Kananian, Hassan Mirnejad, Fatemeh Sepidbar, Ivan Vlastélic, Jean-Louis Paquette, Bernard Barbarin

Zircon U-Pb geochronology, major-trace elements and Sr–Nd isotope geochemistry of Mashhad granodiorites (NE Iran) and their mafic microgranular enclaves: Evidence for magma mixing and mingling

Journal:	*International Geology Review*
Manuscript ID	TIGR-2018-0274.R4
Manuscript Type:	Special Issue
Date Submitted by the Author:	19-Mar-2019
Complete List of Authors:	Deyhimi, Maryam; University of Tehran, Department of Geology Kananian, Ali; University of Tehran, Department of Geology Mirnejad, Hassan; University of Tehran, Department of Geology Sepidbar, Fatemeh; University of Tehran, Vlastelic, Ivan; Laboratoire Magmas et Volcans Paquette, Jean-Louis; Laboratoire Magmas et Volcans Barbarin, Bernard; Laboratoire Magmas et Volcans
Keywords:	Mafic microgranular enclaves, Mashhad granodiorite, magma mixing, Paleo-Tethys ocean, NE Iran

Zircon U-Pb geochronology, major-trace elements and Sr–Nd isotope geochemistry of Mashhad granodiorites (NE Iran) and their mafic microgranular enclaves: Evidence for magma mixing and mingling

Maryam Deyhimi[a], Ali Kananian[a], Hassan Mirnejad[a,b*], Fatemeh Sepidbar[a,c], Ivan Vlastelic[d], Jean-Louis Paquette[d], Bernard Barbarin[d].

[a]*School of Geology, College of Science, University of Tehran, Tehran, Iran*

[b]*Department of Geology and Environmental Earth Sciences, Miami University, Ohio, USA*

[c]*School of Earth Sciences, Damghan University, Damghan 36716-41167, Iran*

[d]*Laboratoire Magmas & Volcans Clermont-Ferrand, France*

[*]*Corresponding author. hmirnejad@ut.ac.ir*

Abstract

Mashhad granitoids and associated mafic microgranular enclaves (MMEs), in NE Iran record late early Mesozoic magmatism which was related to the Paleo-Tethys closure and Iran-Eurasia collision. These represent ideal rocks to explore magmatic processes associated with Late Triassic closure of the Paleo-Tethyan ocean and post-collisional magmatism. In this study, new geochronological data, whole-rock geochemistry, and Sr-Nd isotope data are presented for Mashhad granitoids and MMEs. LA–ICP–MS U-Pb dating of zircon yields crystallisation ages of 205.0±1.3 Ma for the MMEs, indicating their formation during the Late Triassic. This age is similar to the host granitoids. Our results including the major and trace elements discrimination diagrams, in combination with field and petrographic observations (such as ellipsoidal MMEs with feldspar megacrysts, disequilibrium textures of plagioclase) as well as mineral chemistry, suggest that MMEs formed by mixing of mafic and felsic magmas. The host granodiorite is a felsic, high K calc-alkaline I-type granitoid, with SiO_2 = 67.5–69.4 wt%, high K_2O (2.4-4.2 wt%), and low Mg# (42.5–50.5). Normalized abundances of LREEs and LILEs are enriched relative to HREEs and HFSEs (e.g. Nb, Ti). Negative values of whole-rock $\varepsilon Nd_{(t)}$ (-3 to -2.3) from granitoids indicate that the precursor magma was generated by partial melting of enriched lithospheric mantle with some contributions from old lower continental crust. In the MMEs, SiO_2 (53.4–58.2 wt%) is lower and Ni (3.9–

49.7 ppm), Cr (0.8–93.9 ppm), Mg# (42.81–62.84), and $\varepsilon Nd_{(t)}$ (-2.3 to +1.4) are higher than those in the host granodiorite, suggesting a greater contribution of mantle-derived mafic melts in the genesis of MMEs.

Keywords: Mafic microgranular enclaves; Mashhad granodiorite; Magma mixing; Paleo-Tethys ocean; NE Iran.

1. Introduction

Mafic microgranular enclaves (MMEs; Didier and Barbarin 1991) are common in most calc-alkaline granitoids (Xiong et al. 2012; Jiang et al. 2013; Chen et al. 2015) and have been documented in most Cordilleran-type granitoid batholiths (e.g. Pitcher 1983; Didier and Barbarin 1991; Barbarin 1999). MMEs have mafic to intermediate compositions, and occur as angular to rounded enclaves within host intrusive rocks whose silica contents range from intermediate to felsic. The formation of MMEs has been attributed to mixing and/or mingling of mafic and felsic magmas (e.g. Barbarin 2005; Wang et al. 2012), pieces of refractory rock or of melt residues (e.g. Chappell et al. 1987; Chappell and Wyborn 2012), or as chilled margins or cumulates of early-formed crystals (e.g. Donaire et al. 2005; Shellnutt et al. 2010). Numerous studies have confirmed that MMEs in granitoids are formed due to injection of a mafic magmatic component into a felsic magma chamber via a mixing process (e.g. Blundy and Sparks 1992; Barbarin 2005; Jiang et al. 2013).

The Mashhad granitoids and associated MMEs are part of the Mesozoic granitoids of northwestern Pamir-Mashhad magmatic arc, situated between Mashhad in Iran and Paropamisus Mountains in Afghanistan. These granitoids were formed as a result of the northward subduction of the Paleo-Tethys oceanic lithosphere beneath the Turan plate and during the collision of Iran with Eurasia after the closure of Paleo-Tethys ocean (Golonka 2003; Mirnejad et al. 2013)

(Figure 1). The Mashhad area contains the Mashhad batholith, Dehnow stock and their MMEs (Figure 2; Samadi et al. 2014). Mirnejad et al. (2013) reported three distinct zircon U-Pb ages for the Mashhad granitoids, ranging from 217 to 200 Ma. They believe these ages correspond to subduction of Paleo-Tethys under the Turan plate (Eurasia) which was prevailed during Late Triassic. Karimpour et al. (2010a) obtained U–Pb zircon ages of 215–217 Ma for the isolated and small quartz diorite–tonalite–granodiorite bodies that outcrop in the Dehnow–Vakilabad regions, northwest of the Mashhad batholith. The other U–Pb zircon ages reported by Karimpour et al. (2010b, 2011) and Abbasi (2018) from the main Mashhad batholith are 205.9 ± 4.1 Ma and 200.1 ± 3.8 Ma for the collision- and arc-related granitoids, respectively. However, no data exist on the nature of the relationship between granitoid rocks and their MMEs. The MMEs, which occur with various shapes in Mashhad granitoids, present a unique opportunity to describe the petrogenesis, origin and geodynamic setting of granitoid magmas (e.g. Didier and Barbarin 1991; Barbarin 2005; Ventura et al. 2006). MMEs can also provide evidence for crust–mantle interaction, which is not available from their host granitoids (e.g. Griffin et al. 2002; Zhao et al. 2012). Thus, a detailed study of MMEs in the Mashhad granodiorite can improve our understanding of igneous processes related to the Paleo-Tethys subduction. This paper reports new zircon U–Pb ages, whole-rock chemical compositions, and Sr–Nd isotope data from MMEs and their host granodiorite in the Mashhad batholith. Our findings, placed in the context of other published tectonomagmatic data and stratigraphic relationships in the region, offer insight about the nature and genesis of MMEs and associated host granodiorite as well as their tectonic significance during the closure of the Paleo-Tethys ocean.

2. Geologic setting, field observations and petrologic descriptions

During the Late Paleozoic and early Mesozoic eras, a north-dipping subduction zone was present at the southern boundary of the Turan platform (Eurasia), resulting in an extensive magmatic arc that stretched from what is today the Greater Caucasus through the Paropamisus Range, and into the northern Pamir Mountains (Figure 1(a)) (Aharipour et al. 2010; Rossetti et al. 2017; Shafaii Moghadam et al. 2017). It has been proposed that drifting of a series of continental blocks such as Lhasa, Turan, etc. from Gondwana and their collision with Eurasia during Late Paleozoic-early Mesozoic led to the establishment of the Paleo-Tethys orogenic belt throughout the southern margin of Eurasia (Zanchetta et al. 2009). The Paleo-Tethys orogenic belt extends into northern Iran, along the Alborz Mountains from the Binalood Mountains in the east to the Talysh Mountains in the west (Figure 1(b)) (Alavi 1991; Zanchetta et al. 2009).

The Mashhad area in northeastern Iran records the geodynamic evolution of the Paleo-Tethys orogenic belt in the western Pamir-Mashhad magmatic arc (Alavi 1991; Zanchi et al. 2009), which consists of three parallel NW-SE zones: (1) Kopet Dagh, (2) a transitional zone and (3) Binalood (Alavi 1991; Samadi et al. 2014) (Figure 1(b)). The transitional zone, situated between Binalood and Kopet Dagh (Figure 1(b)), was formed by collision between the Eurasian Turan domain in the north, and a Gondwana-derived central Iran block in the south (Alavi 1991; Mirnejad et al. 2013; Samadi et al. 2014). Late Neoproterozoic crust has also been reported in the transitional zone, between the Gondwana and Turan plates (Ghavi et al. 2018).

The Mashhad granodiorite (59°22′-59°45′N, 36°00′-36°22′E) intruded into the transitional zone along major faults of the Paleo-Tethys suture. The oldest units (Figure 2) comprise Late Paleozoic Mashhad–Fariman ophiolites, including ultramafic to mafic-ultramafic lavas, isotropic gabbros, pelagic limestone, interbedded radiolarite, phyllite, and slate (interpreted as an accretionary prism) (Alavi 1991; Ghazi et al. 2001). They are unconformably overlain by Upper

Triassic to Jurassic siliciclastic deposits including quartz conglomerate, sandstone, crystallized limestone, shale, and phyllite (Figure 2) (Alavi 1991; Eftekharnezhad and Behrozi 1991). $^{40}Ar/^{39}Ar$ dating of hornblende gabbros in the Mashhad ophiolite, near Mashhad granitoids (Figure 2(a) and (b)) provides ages of ca. 288 to 282 Ma (Ghazi et al. 2001). The Mashhad batholith consists of three distinct granitoid intrusions: (1) a quartz diorite–tonalite–granodiorite emplaced from 217 ± 4 to 215 ± 4 Ma (Karimpour et al. 2010), (2) a second granodiorite from 212.0 ± 5.2 to 200.1 ± 3.8 Ma (Mirnejad et al. 2013; Abbasi 2018), and (3) a monzogranite intrusion around 199.8 ± 3.7 Ma (Mirnejad et al. 2013). They were intruded into Late Paleozoic metamorphic rocks in the northwestern Mashhad ophiolite (Figures 1(b) and 2) which resulted in a narrow contact metamorphic aureole consisting of almandine- and andalusite-rich pelites, quartzite, and calc-silicate rocks (Iranmanesh and Sethna 1998). The aforementioned rocks are overlain by Cretaceous conglomerate, arkose, and limestone (Figure 2). The NW-SE trend of the Mashhad granodiorite (Figure 2(a)) agrees with emplacement of the Mashhad granitoids during NE-SW directed extension and major faults relating to the Paleo-Tethys suture. The granodiorites are volumetrically the most important part of the granitoids, and contain abundant MMEs (Figure 3), which are scarce or absent in the quartz diorite, and monzogranite.

Abundant MMEs in the granodiorite have rounded to ellipsoidal forms that range in size from 4 cm to 5 m on their longest axis (Figure 3(a-c)). Rare small sigmoidal and elongated enclaves occur locally, reflecting deformation during flow of the host magma (Figure 3(b)). In some places, MMEs with massive (Figure 3(c)) and banded structures (Figure 3(d)), or with linear (Figure 3(e)) or irregular boundaries (Figure 3(f)) enriched in fine-grained mafic material, are present in the host rocks. The MMEs are abundant, mostly dark-colored, fine-grained, and generally massive and show variable shapes (e.g. rounded, oval, ellipsoidal) (Figure 3). Notably,

enclaves partially enclose megacrysts of the host rocks (Figure 3(g)), and MMEs intruded by granitoid magma are common. Margins of some MMEs exhibit a light-coloured zone enriched in feldspar (Figure 3(h)).

3. Petrography

The host granodiorite has a medium-grained, holocrystalline texture and contains mainly euhedral to subhedral phenocrysts of K–feldspar (30–42%), plagioclase (~35%), quartz (15–25%), and amphibole and/or biotite (4–5%) (Figure 4(a)). Subhedral to anhedral K–feldspar (0.5–2 mm) is mostly perthitic. Plagioclase occurs as subhedral to anhedral crystals with compositions ranging from andesine to oligoclase. Magnetite, ilmenite, zircon, apatite ± titanite are the principal accessory minerals.

MMEs generally contain the same mineral assemblage but with higher contents of amphibole, biotite and plagioclase, and lower contents of quartz and K-feldspar. They contain plagioclase (50-56%), K-feldspar (10-16%), hornblende (23-26%), biotite (15-20%), minor quartz, and accessory magnetite, needle-shaped apatite, titanite, and zircon. The textures vary from fine-grained to porphyritic (Figure 4(b)). Plagioclase occurs as either large megacrysts (Figure 4(c)), or as elongated laths within large megacrysts (Figure 4(d)) possibly with complex oscillatory zoning (Figure 4(e)). Minor quartz occurs either as megacrysts or as anhedral crystals that are interstitial to other minerals (Figure 4(f)). Hornblende and biotite are the most abundant mafic minerals in the MMEs, occurring as subhedral to anhedral grains (Figure 4(b,e)), or as anhedral crystals interstitial to plagioclase (Figure 4(f)). Biotite shows greenish brown to reddish-brown pleochroism. Apatite, a common accessory mineral in the MMEs, occurs as acicular crystals (Figure 4(c)).

4. Sampling and analytical methods

Two hundred samples were collected from MMEs and their host granodiorite. From these samples, 140 representative thin sections were prepared and studied by optical microscopy as a basis to select the most suitable samples for geochemical and isotopic analyses. Mineral chemistry analyses for selected minerals of the enclaves and the host granodiorite were performed using the JEOL JXA-8530F field-emission electron microprobe at the Laboratoire Magmas & Volcans (LMV), Clermont–Ferrand, France. The minerals were analyzed at an accelerating voltage of 15 kV using a 10 nA probe current with a spot size of 2 µm to reduce volatilization. Matrix corrections were performed using the ZAF correction scheme.

Major- and trace-element contents of the twenty-five samples were measured at the Laboratoire Magmas & Volcans (LMV) in Clermont–Ferrand, France. For major element analysis, powdered samples (100 mg) were mixed with 300 mg of $LiBO_2$ in a graphite crucible and melted in an induction oven at 1050 °C for 4 minutes. The glass bead was then dissolved in dilute nitric acid, and the resulting solution was further diluted to reach a dilution factor of 2000 (solution/rock weight ratio). The final solutions were analysed by inductively-coupled-plasma-optical-emission-spectrometry (ICP-OES, HORIBA Jobin Yvon Ultima C). Trace element and Sr-Nd isotope analysis were performed on the same dissolution: 50 mg of powder were mixed with 200 mg of purified ammonium bifluoride (NH_4HF_2) in 5 ml Savillex screw-top Teflon vials and placed in an oven at 230°C for 24 hours, which ensures total dissolution of the most resistant minerals. Once cooled, the excess of digestion reagent was eliminated by adding and evaporating 2 ml of 7M HNO_3. The final residue was then totally dissolved in ca. 20-24 g of 7M HNO_3. An aliquot of this solution (0.5 g hosting ca. 1 mg of rock) was diluted by a factor of ca. 12 with 0.05M HF to reach a rock dilution factor between 5000 and 6000, and trace element abundances

were determined by inductively coupled-plasma mass spectroscopy (ICPMS, Agilent 7500). The analyses were performed in plasma robust mode (1550 W). The reaction cell (He mode) was used to reduce interferences on masses ranging from 45 (Sc) to 75 (As). The signal was calibrated externally (every 4 samples) with the BE-N basaltic standard (CRPG Nancy) dissolved in the same manner as the samples, and using the recommended elemental values of Chauvel et al. (2011). The external reproducibility (2σ error) of the method is 6% or less for lithophile elements (K, Rb, Ba, …) and 15% or less for chalcophile elements (Pb, Cu, As, …). Three analyses of the USGS G2 granite standard yielded concentrations that agree, within error, with the GeoRem recommended values (http://georem.mpch-mainz.gwdg.de/).

The remaining solution was reserved for Sr and Nd isotope analysis. After evaporation, samples were taken up in 6 M HCl and evaporated before final dissolution in 1.25 M HCl. Iron was removed from the samples using a strong cation exchanger (Bio-Rad AG50-X4, 200-400 mesh) (Pin and Zalduegui 1997). A tandem column elution scheme using Sr.Spec and Tru.Spec chromatographic materials was then used to achieve the concomitant separation of Sr and LREE (Pin et al. 1994). Nd was then purified from the adjacent lanthanides, especially Sm, using the Ln.Spec chromatographic material (Pin and Zalduegui 1997). The isotopic compositions were analyzed on a TRITON thermal ionisation mass spectrometer (for Sr) and a NEPTUNE plasma source mass spectrometer (for Nd), either in static or dynamic mode. $^{87}Sr/^{86}Sr$ and $^{143}Nd/^{144}Nd$ ratios were normalized to $^{86}Sr/^{88}Sr = 0.1194$ and $^{146}Nd/^{144}Nd = 0.7219$, respectively. Sr and Nd isotope ratios were further normalized relative to $^{87}Sr/^{86}Sr = 0.710245 \pm 13$ (2 SD, 12 measurements) for NBS SRM 987, and to $^{143}Nd/^{144}Nd = 0.512115 \pm 20$ (2 SD, 7 measurements) for JNdi. Initial $^{87}Sr/^{86}Sr$ and $^{143}Nd/^{144}Nd$ were subsequently obtained by back-calculation to ages of igneous crystallization determined by U-Pb on zircon.

U–Th–Pb isotope data on zircon grains were obtained at the Laboratoire Magmas & Volcans (LMV), Clermont–Ferrand, France by Laser-Ablation Inductively-Coupled Plasma Mass-Spectrometry (LA-ICP-MS) with a Thermo Element XR Sector Field high-resolution ICP-MS, coupled to a Resonetics M50E 193 nm excimer laser system. The analytical method for isotope dating with LA-ICP-MS is detailed in Mullen et al. (2018).

5. Analytical Results

5.1 Mineral chemistry

Representative chemical compositions of plagioclase, biotite and amphibole from the granodiorite and associated MMEs are given in Supplementary Table 1. Plagioclase from the Mashhad MMEs are albite-andesine in composition (An = 10.0%–31.6%). Plagioclases are zoned, with a core of albitic composition and relative low An content (10.0%). The An content of plagioclases shows a distinct increase to 31.6% in the rim with a rhythmic zonation, indicating a reverse and complex oscillatory zonings (Figure 5a).

The Mg cations of biotite in granodiorite and MMEs are 1.8-2.5 and 1.5-3.4 atoms per formula unit (a.p.f.u.), whereas their Fe^{2+} cations are 2.2-2.7 and 1.7-2.7 a.p.f.u., respectively. Biotites from granitoids have X_{Mg} (Mg/Mg + Fe) and Ti cations ranging from 0.41 to 0.52 and 0.19 to 0.41 a.p.f.u., respectively, while those from MMEs range from 0.35-0.65 and 0.11-0.43 a.p.f.u, respectively. The amphiboles are characterized by low TiO_2 (0.097-1.36 wt. %) and alkali (Na_2O + K_2O) contents (0.60-3.24 wt. %). The amphibole crystals in the enclaves usually have higher MgO and lower FeO_T contents than those in the host granodiorite (Supplementary Table 1). The amphiboles in the granodiorite and its MMEs have high Ca_B values of 1.66–1.96, low Na_B values

of 0.23–0.52, and moderate Mg# values of 41.29–58.85, indicating they have mainly calcic and ferrohornblendes to magnesiohornblende composition (Figure 5(e)).

5.2 Bulk-rock major and trace elements

Supplementary Table 2 provides whole-rock chemical compositions of representative (twenty-five) samples from Mashhad granodiorite and its MMEs. The granodiorite shows a restricted range in terms of major and trace element concentrations (Supplementary Table 2). It has moderate SiO_2 (67.5–69.4 wt%), Al_2O_3 (15.2–17.6 wt%), Na_2O (3.5–6.2 wt%) and K_2O (2.4–4.2 wt%), and low MgO (0.9–1.6 wt%) contents. Bulk-rock compositions are mainly granodiorite (Figure 6(a)). In the quartz-alkali feldspar-plagioclase (QAP) diagram after (Streckeisen 1979), the Mashhad intrusive rocks show granodiorite to monzogranite compositions (Figure 6b), with high K calc-alkaline affinity (Figure 6(c)). Granodiorite is metaluminous to weakly peraluminous with A/CNK [molar Al_2O_3 / (CaO + Na_2O + K_2O)] less than 1.2 (i.e., regarded as an upper limit for I-type granites as proposed by Chappell (1974) (Figure 6(d)).

Relative to the host granodiorite, the MMEs exhibit more variable SiO_2 (47.98–65.97 wt%), K_2O (1.96–3.53 wt%) and Al_2O_3 (11.66–19.42 wt%), and higher MgO (1.43–6.00 wt%) and Na_2O (2.01–6.60 wt%) contents. In a SiO_2 vs. Na_2O + K_2O classification diagram, MME compositions fall in monzonite, monzodiorite, or diorite fields (Figures 6(a, b)), and high-K calc-alkaline to shoshonite compositions on a K_2O vs. SiO_2 diagram (Figure 6(c)). Accordingly, the MMEs, with intermediate composition, range from metaluminous to slightly peraluminous, with an alumina-saturation index below 1.2 (Figure 6(d)).

Figures 7(a) and (b) exhibit chondrite-normalized REE patterns for Mashhad granodiorite and its MMEs (Sun and McDonough 1989). REE patterns for the Mashhad granodiorite show

enrichment in light REEs (LREEs) compared to heavy REEs (HREEs) ((La/Yb)$_n$=13.67–62.26) and minor negative Eu anomalies (Eu/Eu*=0.84–0.90). MMEs show LREE-fractionated patterns with (La/Yb)$_n$=15.77–70.31 and slightly steeper patterns relative to host granodiorite. Total REE concentrations in granodiorite range from 198 to 370 ppm, while those from MMEs vary from 235 to 720 ppm. The primitive mantle-normalized (Sun and McDonough 1989) multi-element variation diagrams of the granodiorite and associated MMEs from the Mashhad (Figure 7 (c) and (d)) resemble those of arc-related magmas (Pearce and Peate, 1995) with enrichments in large-ion lithophile elements (LILEs; e.g. Rb, Ba and Sr), relative to high field strength elements (HFSEs; i.e., Nb, P and Ti) and HREEs (i.e., Yb). The studied granodiorite and MMEs display marked negative Nb, Zr, P, and Ti anomalies and a positive Sr anomaly relative to the primitive mantle (Figure 7).

When plotted on Harker diagrams, data for the granodiorite and MMEs exhibit negative correlations of Al_2O_3, CaO, Fe_2O_3, MgO, TiO_2, P_2O_5, Mg#, La, and a positive correlation of Pb (Figure 8).

5.3 U-Pb geochronology

Supplementary Table 3 and Figures 9 and 10 display cathodoluminescence (CL) images and U–Pb isotope data of selected zircon grains from MMEs, respectively. Zircon grains are typically colorless, euhedral to subhedral prismatic in form, and exhibit regular concentric zonation in CL images (Figure 9). Grain lengths range from 100 to 200 μm, with length:width ratios between 1:1 and 2:1. U and Th contents of these zircons range from 383–1575 ppm and 12–2948 ppm, respectively, and their Th/U ratios vary between 0.02 and 2.30 with a mean value of 0.5. U-Pb isotope data for thirty MME grains give weighted mean ages of 205.0 ± 1.3 Ma (MSWD = 0.14)

(Figure 10). This date, considered to be the age of MMEs, falls in the age interval of the granitoid (217 to 200 Ma; Karimpour et al. 2010b, 2011; Mirnejad et al. 2013; Abbasi 2018).

5.4 Bulk-rock Sr–Nd isotopes

Supplementary Table 4 lists Sr and Nd isotope data for the Mashhad granodiorite and MMEs. Initial $^{87}Sr/^{86}Sr$ and $^{143}Nd/^{144}Nd$ are calculated based on the average age of the studied samples. In granodiorite, $^{87}Sr/^{86}Sr$ and $^{143}Nd/^{144}Nd$ occupy extremely narrow ranges from 0.7057 to 0.7059 and 0.51222 to 0.51225, respectively. Correspondingly, $\varepsilon Nd_{(t)}$ values are tightly grouped between -3 and -2.3. The MMEs display similar restricted initial $^{87}Sr/^{86}Sr$ (0.7057 to 0.7061), but slightly higher initial $^{143}Nd/^{144}Nd$ (0.51226 to 0.51230), and $\varepsilon Nd_{(t)}$ (–2.3 to -1.4) relative to host granodiorite. The Mashhad granodiorite and MMEs lie on the mantle array and in the enriched quadrant on $^{87}Sr/^{86}Sr$ vs. $\varepsilon Nd_{(t)}$ diagram (Figure 11). These resemble values for Triassic granitoids and associated MMEs of the western Kunlun orogeny (Jiang et al. 2013), East Kunlun Orogen (Xia et al. 2015) and Tagong pluton in Songpan–Ganze terrane (Chen et al. 2017) from the eastern part of the Paleo-Tethys suture zone in China, and are different from the primitive mafic and ultramafic rocks from the Mashhad ophiolite (Shafaii Moghadam et al. 2015), whose isotopic composition is similar to Pacific N-MORB (Figure 11).

6. Discussion

6.1 Implications for magma mixing

MMEs are suitable tracers to understand the petrogenesis and origin of magmas (e.g. Barbarin 2005; Yang et al. 2015). Several hypotheses have been suggested for the origin of MMEs, the most common ones being that they represent restites from the granite source (Chappell et al. 1987), cognate fragments or early-formed crystals from the host magma (e.g. Donaire et al.

2005; Shellnutt et al. 2010), xenoliths (Maas et al. 1997) or mafic magma that was injected and mixed with host felsic magma (Griffin et al. 2002; Barbarin 2005). In the restite model, it has been suggested that enclaves are refractory solid residues of partial melting from the source region (e.g. Chappell 1996; Barbarin and Didier 1992; Chappell et al. 2000). Therefore, they must be older than the host rocks (Liu et al. 2013). Our new and compiled zircon U-Pb ages show the Mashhad MMEs (205 ± 1.3 Ma) are identical to the age of host granitoids (217 to 200 Ma; Karimpour et al. 2010b, 2011; Mirnejad et al. 2013; Abbasi 2018). They also have fine-grained textures relative to the host granitoids without recrystallization, deformation, and metamorphic or residual sedimentary fabrics, which preclude "residues" model. The MMEs from the granodiorites have distinct contacts with their host rocks (Figure 3), and include chilled margins against granodiorites, which is in agreement with magma mixing model. In addition, due to the absence of angular enclaves (Figure 3), cognate model is thus dismissed. Moreover, Vernon (1983) proposed that early-formed minerals by fractional crystallization are commonly coarse grained with euhedral shapes and lack of cumulate textures in the MMEs. Therefore, we propose that the Mashhad MMEs are not mafic mineral cumulates and therefore, a cognate model is ruled out.

Field and petrological observations include: (i) banded structures (Figure 3(d)), and the presence of irregular, fine-grained mafic material in host granodiorite rocks (Blundy and Sparks 1992; Barbarin 2005); (ii) spheroidal to ellipsoidal/ovoidal shapes of enclaves (Figure 3 (g, h)) that resemble pillows of undisputed injection origin in other plutons ((Baxter and Feely 2002; Liu et al. 2013); (iii) enclaves partially enclose megacrysts of the host rocks (Figure 3(g)), suggesting the intermingling of two magmas (Liu et al. 2013) (iv) Feldspar-rich zones at contacts (Liu et al. 2013) (Figure 3(h)); (v) acicular apatite and the presence of resorption surfaces in plagioclase

(Figure 4(c)) and small plagioclase inclusions in a larger plagioclase (Figure 4(d)); (vi) complex oscillatory zoning (Figure 4(e)), with repeated resorption surfaces, marking changes in plagioclase stability brought about by magma mixing (Müller et al. 2005) and (vii) inclusions of biotite and hornblende in plagioclase (Figure 4(f)) (Baxter and Feely. 2002) are evidence for chemical or thermal changes in the melt during crystal growth due to magma mixing.

Composition of amphibole, biotite and plagioclase can be used to distinguish magma sources. The reverse zoning of plagioclases from the MMEs is a disequilibrium texture that indicates magma mixing (Fig. 5a). In the TiO_2–FeO_{total}–MgO diagram, biotites show geochemical similarities to the re-equilibrated to primary biotites (Figure 5(b)) as well as calc-alkaline rocks (Figure5(c)). Moreover, in the TFeO/(TFeO+MgO) versus MgO diagram (after Zhou 1986), granodiorites and MMEs seems to be crystallized from a melt with crust to mantle geochemical signatures (Figure5(d)). This idea is also confirmed with the biotite chemistry, in a Ca–Fe_{tot}–Mg discrimination diagram (after Xie and Zhang (1990). Moreover, the composition of biotites in the enclaves is similar to those in the host which confirms enclaves generated by magma mixing during extensive equilibration processes. We believe these observations are not compatible with a cognate model which proposed by Didier and Barbarin (1991) for the formation of MMEs. Almost all the amphibole and biotite data plot in the crust-mantle mixed category (Figure 5 (d-f)). These features imply that the granodioritic magma and its MMEs were derived from mantle and mixed with crustal components during the mixing/mingling process. Moreover, the geochemical characteristics of the Mashhad granitoids show a linear relationship between major and trace elements and SiO_2 content for both the MMEs and their host granodiorite relative to mafic end-member reported by Shafaii Moghadam et al. 2015 (Figure 8), which can be interpreted as the product of magma mixing (Castro et al. 1990; Chappell 1996; Chen et al.

2017). It should be mentioned that these features (Figure 8) may also be associated with crystallization fractionation (He et al. 2018). However, the role of a fractional crystallization trend of basaltic magma can be excluded for the formation of MME magmas, as they plot near the magma mixing line in the $(Fe_2O_3)_T$–MgO and $\varepsilon Nd_{(t)}$-SiO_2 diagrams (e.g. basaltic and felsic; Castro et al. 1990; Chappell 1996) (Figure 12(a,b)). Shafaii Moghadam et al. (2015), on the basis of Hf isotope data and whole-rock Sr–Nd–Pb isotopic results for the basaltic rocks of Mashhad, suggest the MME magmas were generated from depleted mantle-derived magmas, which conferred primitive signatures of initial $^{87}Sr/^{86}Sr$ = 0.703-0.704 and $\varepsilon Nd_{(t)}$ = +3.7-5.4.

Element-ratio/element-ratio and element/element-ratio plots can support a mixing process if the data plot on a hyperbolic curve in a geochemical discrimination diagram (Langmuir et al. 1978; Blundy and Sparks 1992; Zhou 1994) as noted, for example, in certain suites in the Muchen pluton, China (Liu et al. 2013) (Figure 12(c,d)).

The studied MMEs show similarity in the whole-rock $^{87}Sr/^{86}Sr$ (0.70575-0.70618) isotopic compositions with respect to host granodiorite (0.70578-0.70593), which can be interpreted as chemical and radiogenic isotopic equilibrium during magma mixing (Lesher 1990; Poli et al. 1996) and/or origination from the same source without isotopic fractionation during magma mixing. In addition, MMEs and granodiorite have similar whole-rock $^{143}Nd/^{144}Nd$. However, the MMEs have relatively higher $^{143}Nd/^{144}Nd$ (0.51226-0.512230) than those of the host granodiorite ($^{143}Nd/^{144}Nd$ = 0.51222-0.51225), with εNd(t) differences of up to 1–2 units. Lesher (1990) and Poli et al. (1996) suggested that isotopes of an element are more readily equilibrated and homogenized during a mixing process than are bulk major elements. Furthermore, Holden et al. (1991) proposed that Sr isotopes are equilibrated and homogenized more quickly than Nd isotopes, which is in agreement with Sr and Nd isotopic results for the Mashhad MMEs and

associated host granodiorite. In fact, when a more mafic magma is injected into a felsic magma chamber and then breaks up into enclaves, both magma mingling and chemical diffusion will change the initial composition of the enclave melt. Major elements such as Al and Si in the silicate melt are network-forming components (mainly in tetrahedral form), and thus it is difficult for them to diffuse and homogenize during magma mixing. However, Ca, Fe and Mg as non-network components have relatively different behavior. Moreover, trace elements and isotopic elements can diffuse more rapidly toward homogeneous compositions after mixing. Consequently, we suggest that the similar trace element and isotopic compositions of the MMEs and host granitoids and differences in major element composition may reflect different diffusion rates and partial re-equilibration of the elements during magma mixing, due to the mixing/mingling process (e.g. Lesher 1990; Xiong et al. 2012; Zhao et al. 2012).

6.2 Origin of granodiorite

The granodiorites from Mashhad that were emplaced in the Late Triassic (217-200 Ma; Karimpour et al. 2010, 2011; Mirnejad et al. 2013; Abbasi 2018) are characterized by relatively high SiO_2 contents compared to the MMEs, and have high-K calc-alkaline and metaluminous to slightly peraluminous geochemical signatures (Figure 6(d)). The P_2O_5 contents of the Mashhad granodiorite vary from 0.2% to 0.5%, and decrease with increasing SiO_2 (Figure 8(f)), similar to I-type granitoids. Moreover, Rb/Sr ratios of up to 0.8 in Mashhad granodiorites are similar to those in I-type granites (<0.9; e.g. Wang et al. 1993). The I-type granitic signatures of Mashhad granodiorites are supported by the presence of hornblende and lack of aluminous primary minerals, such as muscovite, cordierite, tourmaline, andalusite, and garnet, with variable Al_2O_3 (15.16–15.97 wt%), and low K_2O (2.38–4.18 wt%) and Na_2O (3.49–6.18 wt%) (Chappell and White 2001). In addition, their Ba/La (9.99–19.36) is higher, and Nb/La (0.45-0.64) is lower than

those in magmas originating from MORB, OIB, and intra-plate environments (Sun and McDonough 1989).

The geochemical data presented here show that Mashhad granodiorites are I-type, subduction-related calc-alkaline intrusions with isotopic signatures (relatively low $^{87}Sr/^{86}Sr$ ratios of 0.7057–0.7059), indicative of having been derived from the mantle. They are also depleted in Nb–Ti, and somewhat enriched in LILEs (e.g. Rb, Ba and Sr) and LREEs, and have high Ba/Zr ratios (0.30-6.43), similar to arc-like rocks formed in the subduction zone (with calc-alkaline affinity; cf. Pearce and Peate 1995). However, syn- to post-collisional rocks are also characterized by HFSE depletions and LILE enrichments.

The subduction process creates distinctive patterns of LILE/LREE, LILE/HFSE and REE/HFSE (Schiano et al. 1995) because during dehydration of a slab, HFSEs are not fractionated whereas LILEs and LREEs are fractionated (Münker et al. 2004). Taken together, the LILE and LREE patterns are compatible with a subduction-modified lithospheric mantle source (Pearce and Peate 1995). Depletion of HFSE (Nb–Ti) relative to LILEs may be ascribed principally to two processes: (1) the addition of an LILE-enriched, Nb–Ti-poor fluid component derived from the subducted slab to the mantle wedge, which in turn served as a more immediate source of magma or (2) retention of Nb–Ti in amphibole relative to Nb and Ti in other phases in the mantle source. These features argue that a subduction related component is present in the mantle source region (i.e., Pearce and Peate 1995).

A plot of Th/Yb vs. Ta/Yb (Pearce et al. 1990) (Figure 13(a)) confirms enriched features of mantle source in the Mashhad granodiorite. In Figure 13(a), granodiorite data displays a trend sub-parallel to the mantle array, but shifted towards higher Th/Yb ratios, suggesting that the

melt(s) were formed from a source that had been previously metasomatized by fluids derived from a subduction zone. The flat normalized HREE patterns in granodiorite suggest that garnet was a residual phase in the mantle source region. Since Nd is more incompatible than Sm, the granodiorite thus inherited low Sm/Nd ratios (0.13-0.16) consistent with small degrees of partial melting in the presence of garnet. A low degree of partial melting is supported by a negative correlation between La/Yb vs. Sm/Nd (Figure 13(b)) and positive correlation between Th/Yb vs. Ta/Yb (Figure 13(a)). Rb/Sr ratios are regarded as another important tracer of mantle–crust interaction. Mantle rocks have very low Rb/Sr ratios (0.01–0.1), compared to lower continental crust (Rb/Sr = 0.12) and middle continental crust (Rb/Sr = 0.22) (Hofmann 1988; Rudnick and Fountain 1995). The Rb/Sr ratios of the Mashhad granodiorite varies widely between 0.13 and 0.49, much higher than in mantle-derived rocks. Nb/La and Nb/Ce ratios in the mantle are respectively about 1.01 and 0.39 (Sun and McDonough 1989) compared to 0.46 and 0.23 in the crust (Weaver and Tarney 1984). Nb/La and Nb/Ce ratios in Mashhad granodiorite that range, respectively, from 0.45 to 0.65 and 0.26 to 0.35, are similar to crustal ratios. Th/Ta ratios in lower continental crust-derived magma (7.9; Shellnutt et al. 2009) are comparable to those in Mashhad granodiorite (5.18 to 12.03, mean 7.95). A lower Mg# and higher SiO_2 wt.% content in granodiorite, relative to the mantle, point additionally to the involvement of a crustal source in the genesis of the Mashhad granodiorite.

6.3 Origin of MMEs

MMEs from the Mashhad granodiorites most likely represent remnants of a mafic magma injected to a felsic magma. Consequently, they provide the best opportunity to study the source of the mafic magma. The Mashhad MMEs are characterized by lower SiO_2, higher Mg#, and higher MgO, MnO, CaO relative to those in Mashhad granodiorite. These geochemical features

along with low ($^{87}Sr/^{86}Sr$)i (0.7057–0.7061) and high εNd(t) values (-2.1 to -1.4) (Supplementary Table 4; Figure 11) show the MMEs formed from mantle-derived magmas.

The Mashhad MMEs are also characterized by high K to shoshonitic signatures (Figure 6(c)). Previous workers have established that potassic mafic magma end members might be generated from either small degree of partial melting of enriched lithospheric mantle at depths below the level of amphibole stability (Foley and Peccerillo 1992), and/or metasomatic processes in the subduction zone (Edgar et al. 1980). The similarity between the MMEs and Nb enriched arc basalts (NEBs) (Figure 13(c)) and their trends on the Ba/Th vs. Th/Nb plot (Figure 11(d)) imply that a mantle source metasomatized by slab fluids was involved in their petrogenesis. However, the relatively low initial $^{87}Sr/^{86}Sr$ isotope ratios, high La/Nb (1.8 – 4.8) and low La/Ba (0.05 – 0.30) ratios, as well as enrichment of LILE (e.g. Rb, Ba, Th, and K) and LREEs and depletion of HFSEs in the studied MMEs advocates partial melting of an enriched lithospheric mantle metasomatized by slab fluid.

A possible implication of lower crust endmembers can be inferred from trace-element ratios such as Rb/Sr, Nb/La, Nb/Ce, and Th/Ta. The Rb/Sr ratios of the MMEs vary widely between a 0.03 and 0.86, much higher than those in rocks derived from mantle, but similar to these ratios in host granodiorite. Nb/La, and Nb/Ce ratios in the MMEs (0.2–1.19 and 0.09–0.66, respectively) are much higher than those in mantle-derived rocks, suggesting possible participation of a lower crust source in addition to a mantle source. Most of Th/Ta ratios of the MMEs, ranging between 3.89–22.09 (mean, 8.93) show considerable contributions of lower crust materials in the source. Lower Mg# and higher SiO_2 are regarded as crustal geochemical signatures. These data, taken together, imply the involvement of both lower crust and an enriched lithospheric mantle that had been metasomatized by subducted slab fluid or/and decompression melting of enriched

lithospheric mantle metasomatized by previous slab fluids following the post-orogenic collapse extension (Barbarin 1999). However, in diagrams of Rb vs. Yb+Ta (Pearce et al. 1984) and R2 (6Ca + 2Mg + Al) vs. R1 (4Si - 11(Na + K) - 2(Fe + Ti)) (Batchelor and Bodwen 1985), the data plot in the uppermost corner of the volcanic arc granite and pre-collision to syn-collision fields (Figure 6(e, f)).

6.4 Geodynamic implications

The Pamir-Mashhad magmatic arc consists of a Mesozoic east–west-trending magmatic belt (Figure 1). This belt developed in response to the subduction of the Paleo-Tethyan plate beneath the Eurasian plate. Triassic igneous rocks in the western and central Pamir-Mashhad magmatic arc, including Mashhad granitoids (Karimpour et al. 2010, Mirnejad et al. 2013), Torbat Jam (Ghavi et al. 2018), the Feroz Koh unit, Paropamisus (Debon et al. 1987); Hindu Kush, Western Badakhshan (Debon et al. 1987) and central Badakhshan (Desio 1964) are related to the northward subduction of the Paleo-Tethys ocean under the southern Eurasian plate margin. Ages of the MMEs fall in the age interval of the Late Triassic Mashhad granitoids (217-200 Ma; Karimpour et al. 2010, 2011; Mirnejad et al. 2013; Abbasi 2018), Kashafroud granodiorite (210.9 ± 2.5 Ma; Zanchetta et al. 2013), Torbat Jam granites (217 ± 1.7 Ma; Zanchetta et al. 2013). These ages from the granitoids suggest that plutonism has occurred from ~217 to 200 Ma in the Mashhad. LA–ICP–MS zircon U-Pb dating indicates that the Mashhad MMEs crystallised at 205±1.3 Ma. These ages clearly show that the MMEs and the host granodiorite were formed during the Late Triassic.

The Sr–Nd isotopic signatures and trace element characteristics and mineral chemistry of the Mashhad granodiorite and its MMEs show interaction of the mantle–derived melts with

continental crust during ascent, storage and evolution of the Mashhad magmas. Isotopically, the mantle–derived melts would be similar to the melts of the Mashhad ophiolite in the south of Mashhad granodiorite (Figure 2). Previous studies show that gabbro of Mashhad ophiolites have $^{40}Ar/^{39}Ar$ plateau ages of 281–277 Ma (Late Pennsylvanian – Early Permian; Ghazi et al. 2001), similar to other ages for Paleo-Tethys oceanic crust (Ghazi et al. 2001). Shafaii Moghadam et al. (2015), on the basis of Hf isotope data and whole-rock Sr–Nd–Pb isotopic results, suggested that magma of the gabbroic and basaltic rocks were generated from depleted mantle-derived magmas, which conferred primitive signatures of initial $^{87}Sr/^{86}Sr$ = 0.703-0.704 and $\varepsilon Nd_{(t)}$ = +3.7-+5.4, that was either affected by subducted sediments or was contaminated by continental crust.

Mashhad granodiorite and associated MMEs are located at the transitional zone (Figure 1(b)). Ghavi et al. (2018) suggested that the Kope-Dagh and transitional zone (Figure 1(b)) belong to Gondwana-derived blocks, which are characterized by a Neoproterozoic crust, and perhaps the Turan plate consists mostly of early Neoproterozoic crust. Therefore, the continental crust involved might be Neoproterozoic lower crust with initial $^{87}Sr/^{86}Sr$ = 0.714 (Shafaii Moghadam et al. 2015).

When closure of Paleo-Tethys began in early Carnian time (c.a. 225 Ma), the northern margin of the Iran plate changed into a peripheral foreland basin (Zanchetta et al. 2013). In the Rb vs. Y + Ta and R2 vs. R1 diagrams (Figure 6(e,f)), data from the granodiorite plot between the uppermost corner of the volcanic arc granitoids, pre-collision setting, to syn-collision granitoids fields, suggesting that they may be generated in a pre-collisional (subduction-related) to collisional arc setting. These late Triassic ages, ranging from 217 to 200 Ma (Karimpour et al. 2010, 2011; Zanchetta et al. 2013; Mirnejad et al. 2013; Abbasi 2018), and the MME enclave age (205 Ma), pertain to arc-related granodioritic rocks (Mashhad and to surrounding areas including

Torbat Jam, the and Kashafroud Formation), all of them formed during continental collision between the Iran and Turan plates through a subduction to collisional setting.

At the end of subduction of the Paleo-Tethyan ocean (~225 Ma), the continent-continent collision between the Eurasian (Turan) and Iran plates (c.a. 225 Ma) took place, accompanied by crustal thickening (Zanchi et al. 2006; Wilmsen et al. 2009). The extension following crustal thickening led to decompression melting of enriched lithospheric mantle, which is metasomatized by previous slab fluids. The extension following the collision-collision continental crust can be confirmed by the occurrence of extensional faulting with NW-SE trending faults (Figure 2). The basaltic melts derived from this metasomatized mantle underplated the overlying mafic lower crust, where magma stayed in the magma chamber and provided heat for partial melting of Neoproterozoic lower crust. Underplating of basaltic magma under lower crust can be established by existence of basic rocks from Mashhad ophiolites, which have primitive isotopic signatures (initial $^{87}Sr/^{86}Sr$ =0.703; Shafaii Moghadam et al. 2015). This basic magma underplated the lower crust, and produced partial melts of felsic composition, which formed the Mashhad calc-alkaline granodiorite with mixed mantle component. The mafic magma derived from the enriched lithospheric mantle mixed with the granodioritic magma to form MMEs (Figure 14).

7. Conclusions

(1) U-Pb zircon dating indicates that the Mashhad MMEs crystallized at 205.0 ± 1.3 Ma, implying their formation during the Late Triassic.

(2) Field and petrographic observations, such as ellipsoidal and spherical shapes, K-feldspar megacrysts, the presence of acicular apatite, oscillatory zoned plagioclase, together with mineral

chemistry, geochemical and isotopic evidences indicate that MMEs and associated granodiorite were generated by mixing/mingling of felsic and mafic magmas.

(3) The relatively similar emplacement age and whole-rock $\varepsilon Nd_{(t)}$ values between the calc-alkaline I-type granodiorite and enclosed MMEs indicate that the pluton was generated by the subduction of the Paleo-Tethys oceanic lithosphere beneath the Turan plate during the Late Triassic, but contained various degrees of contributions from an enriched lithospheric mantle and lower crustal components.

8. Acknowledgments

This paper is part of PhD dissertation of the first author, supported financially by Laboratoire Magmas & Volcans Clermont-Ferrand, France. Leon E. Long edited an earlier version of the manuscript to improve English usage and scientific content. We would like to thank H. Shafaii Moghadam for editorial handling of the paper as well as providing insightful scientific guidance, and F. Lucci and two anonymous reviewers for in depth comments, all of which improved this paper significantly.

9. References

Abbasi, Z., 2018, Geochronology and Geochemistry of Isotopic Granitoids in Southern Mashhad (M.Sc. thesis): Damghan University, School of Earth Sciences, 120 p (in Farsi with English abstract).

Abdel-Rahman, A.F.M., 1994, Nature of biotites from alkaline, calc-alkaline, and peraluminous magmas: Journal of petrology, v. 35, p. 525-541.

Aharipour, R., Moussavi, M.R., Mosaddegh, H., and Mistiaen, B., 2010, Facies features and paleoenvironmental reconstruction of the Early to Middle Devonian syn-rift volcano-

sedimentary succession (Padeha Formation) in the Eastern-Alborz Mountains, NE Iran: Facies, v. 56, p. 279-294.

Alavi, M., 1991, Sedimentary and structural characteristics of the Paleo-Tethys remnants in northeastern Iran: The Geological Society of America Bulletin, v. 103,p. 983–992.

Barbarin, B., and Didier, J., 1992, Genesis and evolution of mafic microgranular enclaves through various types of interaction between coexisting felsic and mafic magmas: Earth and Environmental Science Transactions of the Royal Society of Edinburgh, v. 83, p. 145-153.

Barbarin, B., 1999, A review of the relationships between granitoid types, their origins and their geodynamic environments: Lithos, v. 46, p. 605–626.

Barbarin, B., 2005, Mafic magmatic enclaves and mafic rocks associated with some granitoids of the central Sierra Nevada batholith, California: nature, origin, and relations with the hosts: Lithos, v. 88, p. 155–177.

Batchelor, R.A., and Bowden, P., 1985, Petrogenetic interpretation of granitoid rock series using multicationic parameters: Chemical Geology, v. 48, p. 43-55.

Baxter, S., and Feely, M., 2002, Magma mixing and mingling textures in granitoids: examples from the Galway Granite, Connemara, Ireland: Mineralogy and Petrology, v. 76, p. 63–74.

Blundy, J.D., and Sparks, R.S.J., 1992, Petrogenesis of mafic inclusions in granitoids of the Adamello Massif, Italy: Journal of Petrology, v. 33, p. 1039-1104.

Castro, A., Moreno-Ventas, I., and De la Rosa, J.D., 1990, Microgranular enclaves as indicators of hybridization processes in granitoid rocks, Hercynian Belt, Spain: Geological Journal, v. 25, p. 391-404.

Chappell, B.W., 1974, Two contrasting granite types: Pacif. Geol., v. 8, p. 173-174.

Chappell, B.W., White, A.J.R., and Wyborn, D., 1987, The importance of residual source material restite in granite petrogenesis: Journal of Petrology, v. 28, p. 1111–1138.

Chappell, B.W., 1996, Magma mixing and the production of compositional variation within granite suites: evidence from the granites of southeastern Australia: Journal of Petrology, v. 37, p. 449-470.

Chappell, B.W., White, A.J.R., Williams, I.S., Wyborn, D., and Wyborn, L.A.I., 2000, Lachlan Fold Belt granites revisited: high-and low-temperature granites and their implications: Australian Journal of Earth Sciences, v. 47, pp. 123-138.Chappell, B.W., and White, A.J.R., 2001, Two contrasting granite types 25 years later: Australian Journal of Earth Sciences, v. 48, p. 489-499.

Chappell, B.W., and Wyborn, D., 2012, Origin of enclaves in S-type granites of the Lachlan Fold Belt: Lithos, v. 154, p. 235-247.

Chauvel, C., Bureau, S., and Poggi, C., 2011, Comprehensive chemical and isotopic analyses of basalt and sediment reference materials: Geostandards and Geoanalytical Research, v. 35, p. 125-143.

Chen, S., Niu, Y., Sun, W., Zhang, Y., Li, J., Guo, P., and Sun, P., 2015, On the origin of mafic magmatic enclaves (MMEs) in syn-collisional granitoids: evidence from the Baojishan pluton in the North Qilian Orogen, China: Mineralogy and Petrology, v. 109, p. 577-596.

Chen, Q., Sun, M., Zhao, G., Yang, F., Long, X., Li, J., Wang, J., and Yu, Y., 2017, Origin of the mafic microgranular enclaves (MMEs) and their host granitoids from the Tagong pluton in Songpan–Ganze terrane: An igneous response to the closure of the Paleo-Tethys ocean: Lithos, v. 290, p. 1–17.

Debon, F., Afzali, H., Le Fort, P., and Sonet, J., 1987, Major intrusive stages in Afghanistan: typolgy, age and geodynamic setting: Geologische Rundschau, v. 76, p. 245–264.

Desio, A., 1964, Geological tentative map of the WesternKarakorum: Institute of Geology, Milano University, Milano, scale 1/500 000.

Didier, J., and Barbarin, B., 1991, Enclaves and Granite Petrology. Developments in Petrology: Elsevier, Amsterdam, 625 p.

Donaire, T., Pascual, E., Pin, C., and Duthou, J.L., 2005, Microgranular enclaves as evidence of rapid cooling in granitoid rocks: the case of the Los Pedroches granodiorite, Iberian Massif, Spain: Contributions to Mineralogy and Petrology, v. 149,p. 247–265.

Edgar, A.D., Condliffe, E., Barnett, R.L., and Shirran, R.J., 1980, An experimentalstudyof an olivine eugandite magma and mechanisms for the formation of its K-enriched derivatives: Journal of Petrology, v. 21,p. 475- 497.

Eftekharnezhad, J., and Behroozi, A., 1991, Geodynamic significance of recent discoveries of ophiolites and Late Palaeozoic rocks in NE Iran (including Kopet Dagh): Abhandlungen der Geologischen Bundesanstalt, v. 38, p. 89-100.

Foley, S., and Peccerillo, A., 1992, Potassic and ultrapotassic magmas and their origin: Lithos, v. 28, p. 181-185.

Ghazi, M., Hassanipak, A.A., Tucker, P.J., and Mobasher, K., 2001, Geochemistry and ^{40}Ar–^{39}Ar ages of the Mashhad Ophiolite, NE Iran: Eos,.Transactions of the American Geophysical Union 82 (47) (Fall Meet.).

Ghavi, J., Karimpour, M.H., Mazaheri, S.A., and Pan, Y., 2018, Triassic I-type granitoids from the Torbat e Jam area, northeastern Iran: Petrogenesis and implications for Paleotethys tectonics: Journal of Asian Earth Sciences, v. 124, p. 1-74.

Golonka, J., Krobicki, M., Oszczypko, N., Ślączka, A., and Słomka, T., 2003, Geodynamic evolution and palaeogeography of the Polish Carpathians and adjacent areas during Neo-Cimmerian and preceding events (latest Triassic–earliest Cretaceous), in McCann, T., and Saintot, A., Eds., Tracing tectonic deformation using the sedimentary record: Geological Society of London, Special Publication, v. 208, p. 138–158.

Griffin, W.L., Wang, X., Jackson, S.E., Pearson, N.J., O'Reilly, S.Y., Xu, X., and Zhou, X., 2002, Zircon chemistry and magma genesis, SE China: In-situ analysis of Hf isotopes, Tonglu and Pingtan igneous complexes: Lithos, v. 61, p. 3-4.

He, W., Yang, L., Lu, Y., Jeon, H., Xie, S., and Gao, X., 2018, Zircon U–Pb dating, geochemistry and Sr–Nd–Hf–O isotopes for the Baimaxueshan granodiorites and mafic

microgranulars enclaves in the Sanjiang Orogen: Evidence for westward subduction of Paleo-Tethys: Gondwana Research.

Hofmann, A.W., 1988, Chemical differentiation of the Earth: The relationship between mantle, continental crust, and oceanic crust: Earth and Planetary Science Letters, v. 90, p. 297–314.

Holden, P., Halliday, A.N., Stephens, W.E., and Henney, P.J., 1991, Chemical and isotopic evidence for major mass transfer between mafic enclaves and felsic magma: Chemical Geology, v. 92, p. 135 -152.

Iranmanesh, J., and Sethna, S.F., 1998, Petrography and geochemistry of the Mesozoic granite at Mashhad, Khorasan Province, northeastern part of Iran: Geological Society Journal of India, v. 52, p. 87–94.

Jiang, Y.H., Jia, R.Y., Liu, Z., Liao, S.Y., Zhao, P., and Zhou, Q., 2013, Origin of Middle Triassic high-K calc-alkaline granitoids and their potassic microgranular enclaves from the western Kunlun orogen, northwest China: A record of the closure of Paleo- Tethys: Lithos, v. 156, p. 13-30.

Karimpour, M.H., Stern, C.R., Farmer, L., 2010a, Zircon U–Pb geochronology, Sr–Nd isotope analyses, and petrogenetic study of the Dehnow diorite and Kuhsangi granodiorite (Paleo-Tethys), NE Iran: Journal of Asian Earth Sciences, v. 37, p. 384–393.

Karimpour, M.H., Stern, C.R., Farmer, L., 2010b, Geochronology, radiogenic isotope geo chemistry, and petrogenesis of Sangbast Paleo-Tethys monzogranite, Mashhad, Iran: Iranian Journal of Crystallography and Mineralogy, v. 17, p. 706–719.

Karimpour, M.H., Stern, C.R., Farmer, L., 2011, Rb–Sr and Sm–Nd isotopic compositions, U–Pb age and petrogenesis of Khajeh Mourad Paleo-Tethys leucogranite, Mashhad, Iran: Geosciences: Quaternary Journal of the Geological Survey of Iran, v. 20, p. 171–182 (In Farsi).

Kepezhinskas, P.K., Defant, M.J., and Drummond, M.S., 1996, Progressive enrichment of island arc mantle by melt-peridotite interaction inferred from Kamchatka xenoliths: Geochimica et Cosmochimica Acta, v. 60, p. 1217–1229.

Langmuir, C., Vockejr, R., Gilbert, N.H, and Hart, S.R., 1978, A general mixing equation with applications to Icelandic basalts: Earth and Planetary Science Letters, v. 37 p. 380-392.

Leake, B.E., Woolley, A.R., Arps, C.E., Birch, W.D., Gilbert, M.C., Grice, J.D., Hawthorne, F.C., Kato, A., Kisch, H.J., Krivovichev, V.G., and Linthout, K., 1997, Report. Nomenclature of amphiboles: report of the subcommittee on amphiboles of the international mineralogical association commission on new minerals and mineral names: Mineralogical magazine, v. 61, p. 295-321.

Lesher, C.E., 1990, Decoupling of chemical and isotopic exchange during magma mixing: Nature, v. 344, p. 235–237.

Liu, L., Qiu, J.S., and Li, Z., 2013, Origin of mafic microgranular enclaves (MMEs) and their host quartz monzonites from the Muchen pluton in Zhejiang Province, Southeast China: Implications for magma mixing and crust–mantle interaction: Lithos, v. 160, p. 145–163.

Maas, R., Nicholls, I.A., and Legg, C., 1997, Igneous and metamorphic enclaves in the S–type Deddick Granodiorite, Lachlan Fold Belt, SE Australia: petrographic, geochemical and Nd–Sr isotope evidence for crustal melting and magma mixing: Journal of Petrology, v. 38, p. 815-841.

Middlemost, E.A. K., 1994, Naming materials in the magma/igneous system: Earth-Science Reviews, v. 37, p. 215–224.

Miller, J.S., Matzel, J.E.P., Miller, C.F., Burgess, S.D., and Miller, R.B., 2007, Zircon growth and recycling during the assembly of large, composite arc plutons: Journal of Volcanology and Geothermal Research, v. 167, p. 282–299.

Mirnejad, H., Lalonde, A.E., Obeid, M., Hassanzadeh, J., 2013, Geochemistry and petrogenesis of Mashhad granitoids: An insight into the geodynamic history of the Paleo-Tethys in Northeast of Iran: Lithos, v. 170, p. 105-116.

Mullen, E.K., Paquette, J.L., Tepper, J.H., and McCallum, I.S., 2018, Temporal and spatial evolution of the Northern Cascade Arc magmatisme revealed by LA-ICP-MS U-Pb zircon dating: Canadian Journal of Earth Sciences, v. 55, p. 443-462.

Müller, A., Breiter, K., Seltmann, R., and Pécskay, Z., 2005, Quartz and feldspar zoning in the eastern Erzgebirge volcano-plutonic complex (Germany, Czech Republic): evidence of multiple magma mixing: Lithos, v. 80, p.201-227.

Münker, C., Wörner, G., Yogodzinski, G.M., and Churikova, T.G., 2004, Behaviour of high field strength elements in subduction zones: constraints from Kamtchatka–Aleutian arc lavas: Earth and Planetary Science Letters, v. 224, p. 275-293.

Nachit, H., Ibhi, A., Abia, E.H., and Ohoud, M.B., 2005, Discrimination between primary magmatic biotites, reequilibrated biotites and neoformed biotites: Comptes Rendus Geoscience, v. 337, p. 1415-1420.

Natal'in, B.A., and Şengör, A.M.C., 2005, Late Palaeozoic to Triassic evolution of the Turan and Scythian platforms: the pre-history of the Paleo-Tethyan closure: Tectonophysics, v. 404, p. 175–202.

Pearce, J., Bender, J.F., Long, S.E.D., Kidd, W.S.F., Low, P.J., Güner, Y., Saroglu, F., Yilmaz, Y., Moorbath, S., and Mitchell, J.G.,1990, Genesis of collision volcanism in Eastern Anatolia, Turkey: Journal of Volcanology and Geothermal Research,v. 44, p. 189-229.

Pearce, J.A., Harris, N.B.W., and Tindle, A.J., 1984, Trace element discrimination diagrams for the tectonic interpretation of granitic rocks: Journal of Petrology, v. 25, p. 956-83.

Pearce, Julian., and Peate, D.W., 1995, Tectonic Implications of the Composition of Volcanic ARC Magmas: Annual Review of Earth and Planetary Sciences, v. 23, p. 251-285.

Peccerillo, A., and Taylor, S.R., 1976, Geochemistry of Eocene calc-alkaline volcanic rocks from the Kastamonu area, northern Turkey: Contributions to Mineralogy and Petrology, v. 58, p. 63–81.

Pin, C., Briot, D., Bassin, C., and Poitrasson, F., 1994, Concomitant separation of strontium and samarium–neodymium for isotopic analysis in silicate samples, based on specific extraction chromatography: Analytica Chimica Acta, v. 298, p. 209–217.

Pin, C., and Zalduegui, J.S., 1997, Sequential separation of light rare-earth elements, thorium and uranium by miniaturized extraction chromatography: application to isotopic analyses of silicate rocks: Analytica Chimica Acta, v. 339, p. 79–89.

Pitcher, W.S., 1983, Granite Type and Tectonic Environment, in: Hsu, K., Eds., Mountain Building Processes: Academic Press, London, p. 19– 40.

Poli, G., Tommasini, S., and Halliday, A.N., 1996, Trace Elements and Isotopic Exchange During Acid–basic Magma Interaction Proceses: Geological Society of American Special Papers, v. 87, p. 225–232.

Ribeiro, J.M., Stern, R.J., Kelley, K.A., Martinez, F., Ishizuka, O., Manton, W.I., and Ohara, Y., 2013, Nature and distribution of slab-derived fluids and mantle sources beneath the Southeast Mariana forearc rift: Geochemistry, Geophysics, Geosystems, v. 14, p. 4585-4607.

Rossetti, F., Monié, P., Nasrabady, M., Theye, T., Lucci, F. and Saadat, M., 2017, Early Carboniferous subduction-zone metamorphism preserved within the Palaeo-Tethyan Rasht ophiolites (western Alborz, Iran): Journal of the Geological Society, v. 174, p. 741-758.

Rudnick, R.L., and Fountain, D.M., 1995, Nature and composition of the continental crust: a lower crustal perspective: Reviews of Geophysics, v. 33, p. 267-309.

Samadi, R., Gazel, E., Mirnejad, H., Kawabata, H., Baharifar, A.A., and Sheikh Zakariaee., S,J., 2014, Triassic Paleo-Tethys subduction in the center of the Alpine Himalayan Orogen: Evidence from Dehnow I-type granitoids (NE Iran): Neues Jahrbuch für Geologie und Paläontologie-Abhandlungen, v. 271/3, p. 285–306.

Schiano, P., Clocchiatti, R., Shlmizu, N., Maury, R.C., Jwhum, K.P., and Hofmann, A.W., 1995, Hydrous, silica-rich melts in the sub-arc mantle and their relationship with erupted arc lavas. Nature, v. 377, p. 595-600.

Shafaii Moghadam, H., Li, X.H., Ling, X.X., Stern, R.J., ZakiKhedr, M., Massimo Chiaradia, M., Ghorbani, G., Arai, S., and Tamura, A., 2015, Devonian to Permian evolution of the Paleo-Tethys Ocean: New evidence from U–Pb zircon dating and Sr–Nd–Pb isotopes of the Darrehanjir–Mashhad "ophiolites", NE Iran: Gondwana research, v. 28, p. 781-799.

Shafaii Moghadam, H.S., Li, X.H., Santos, J.F., Stern, R.J., Griffin, W.L., Ghorbani, G., and Sarebani, N., 2017, Neoproterozoic magmatic flare-up along the N. margin of Gondwana: The Taknar complex, NE Iran: Earth and Planetary Science Letters, v. 474, p. 83-96.

Shand, S.J., 1943, The eruptive rocks (2nd edition): John Wiley, New York, 444 p.

Shellnutt, G., Zhou, M.F., and Zellmer, G.F., 2009, The role of Fe–Ti oxide crystallization in the formation of A-type granitoids with implications for the Daly gap: An example from the Permian Baima igneous complex, SW China: Chemical Geology, v. 259, p. 204–217.

Shellnutt, J.G., Jahn, B.M., Dostal, J., 2010, Elemental and Sr\Nd isotope geochemistry of microgranular enclaves from peralkaline A-type granitic plutons of the Emeishan large igneous province, SW China: Lithos, v. 119, p. 34–46.

Streckeisen, A., 1979, Classification and nomenclature of volcanic rocks, lamprophyres, carbonatites, and melilitic rocks: Recommendations and suggestions of the IUGS Subcommission on the Systematics of Igneous Rocks: Geology, v. 7, pp. 331-335.

Sun, S.S., and McDonough, W.F., 1989, Chemical and isotopic systematics of oceanic basalts: implications for mantle composition and processes, in Saunders, A.D., and Norry, M.J., Eds., Magmatism in the ocean basins: Geological Society of London, Special Publication, v. 42, p. 313–345.

Ventura, G., Del Gaudio, P., and Iezzi, G., 2006, Enclaves provide new insights on the dynamics of magma mingling: A case study from Salina Island (Southern Tyrrhenian Sea, Italy): Earth and Planetary Science Letters, v. 243, p. 128-140.

Wang, D.R., Xie, Y.M., Hu, Y.J., You, X.X., and Cao, J.X., 1993, Geology of Guogailiang area (Map G-48-1-A): Panxi Geological Team, Geology and Mineral Resources Bureau, Sichuan Province, scale 1:50000.

Wang, J., Diwu, C., Sun, Y., Liu, Y., and Wang, W., 2012, LA-ICP-MS zricon U-Pb dating and Hf isotope analysis of Qinggangping granodiorite in Xixia area of western Henan province and their geological significance: Geochemical Bulletin of China, v. 31, p. 884-895.

Weaver, B.L., and Tarney, J., 1984, Empirical approach to estimating the composition of the continental crust: Nature, v. 310, p. 575-577.

Wilmsen, M., Fürsich, F.T., Seyed-Emami, K., Majidifard, M.R., and Taheri, J., 2009, The Cimmerian Orogeny in northern Iran: Tectono-stratigraphic evidence from the foreland: Terra Nova, v. 21, p. 211-218.

Xia, R., Wang, C.M., Qing, M., Li, W.L., Carranza, E.J.M., Guo, X.D., Ge, L.S., and Zeng, G.Z., 2015, Zircon U–Pb dating, geochemistry and Sr–Nd-Pb–Hf–O isotopes for the Nan'getan granodiorites and mafic microgranular enclaves in the East Kunlun Orogen: record of closure of the Paleo-Tethys: Lithos, v. 234, p. 47–60.

Xie, Y.W., and Zhang, Y. Q.,1990, Peculiarities and genetic significance of hornblende from granite in the Hengduansan region: Acta Mineral Sin (in Chinese), v. 10, p. 35-45.

Xiong, F.H., Ma, C.Q., Zhang, J.Y., and Liu, B., 2012, The origin of mafic microgranular enclaves and their host granodiorites from East Kunlun, Northern Qinghai-Tibet Plateau: implications for magma mixing during subduction of Paleo-Tethyan lithosphere: Mineralogy and Petrology, v. 104, p. 211-224.

Yang, J., Siebert, C., Barling, J., Savage, P., Liang, Y.H., and Halliday, A.N., 2015, Absence of molybdenum isotope fractionation during magmatic differentiation at Hekla volcano, Iceland: Geochimica et Cosmochimica Acta, v. 162, p. 126–136.

Zanchetta, S., Zanchi, A., Villa, I., Poli, S., and Muttoni, G., 2009, The Shanderman eclogites: a late carboniferous high- pressure event in the NW Talesh Mountions (NW Iran): Geological Society of London, Special publications, v. 312, p. 57-78.

Zanchetta, S., Berra, F., Zanchi, A., Bergomi, M., Caridroit, M., Nicora, A., and Heidarzadeh, G., 2013, The record of the Late Palaeozoic active margin of the Palaeotethys

in NE Iran: constraints on the Cimmerian orogeny: Gondwana Research, v. 24, p. 1237–1266.

Zanchi, A., Berra, F., Mattei, M., Ghassemi, M.R., and Sabouri, J., 2006, Inversion tectonics in central Alborz, Iran: Journal of Structural Geology, v. 28, p. 2023-2037.

Zanchi, A., Zanchetta, S., Berra, F., Mattei, M., Garzanti, E., Molyneux, S., Nawab, A., and Sabouri, J., 2009, The Eo-Cimmerian (Late? Triassic) orogeny in North Iran, in Brunet, M.F., Wilmsen, F., and Granath, J.W., Eds., South Caspian to Central Iran basins: Geological Society of London, Special Publication, v. 312, p. 31-55.

Zhao, K.D., Jiang, S.Y., Yang, S.Y., Dai, B.Z., and Lu, J.J., 2012, Mineral chemistry, trace elements and Sr–Nd–Hf isotope geochemistry and petrogenesis of Cailing and Furong granites and mafic enclaves from the Qitianling batholith in the Shi-Hang zone, South China: Gondwana Research, v. 22, p. 310-324.

Zhou, M.F., and Robinson, P.T., 1994, High-Cr and high-Al podiform chromitites, Western China: relationship to partial melting and melt/rock reaction in the upper mantle: International Geology Review, v. 36, p.678-686.

Zhou, Z.X., 1986, The origin of intrusive mass in Fengshandong, Hubei Province: Acta Petrol. Sin. V. 29, p. 59–70 (in Chinese with English abstract).

10. Figure captions

Figure 1. (a) the North Pamir–Mashhad arc passes south of Mashhad city and extends along the Alborz Mountain to southern Azerbaijan (modified after Natal'in and Şengör 2005), and (b) geological map of the Paleo-Tethys orogenic belt in northern Iran (after Zanchi et al. 2009).

Figure 2. Geological map of the Mashhad batholith (modified after Mirnejad et al. 2013).

Figure. 3. Relationships between MMEs and the Mashhad granodiorite host. (a) Cross cutting of rounded to ellipsoid MMEs and host granodiorite by late stage aplitic phase; (b) sigmoidal and

elongated enclaves within Mashhad granodiorite, reflecting deformations during flow of the host magma; A view of (c) massive; (d) banded structures; (e) liner and (f) irregular boundaries patches enriched in fine-grained mafic material in the granodiorite host rocks; (g) Enclosing of feldspar megacrysts from the host by enclaves and (h) Enclosing of enclaves by feldspar megacrysts from the host.

Figure 4. Thin section photographs (cross-polarised light) of representative MMEs from the Mashhad granodiorite. (a) Granular texture in the granodiorite with associated minerals; (b) Microgranular texture in the MMEs with associated minerals; (c) Acicular apatite in the plagioclase with resorption texture in the MMEs; (d) small lath-shaped plagioclase inclusions hosted by a large plagioclase in the MMEs; (e) oscillatory zoning in the plagioclase from MMEs; (f) inclusions of quartz, biotite and hornblende in plagioclase. Abbreviations: Amp = amphibole; Ap = Apatite; Bi = biotite; K-fls = K-feldspar; Plg = plagioclase; Qtz = quartz.

Figure 5. Compositional plots of plagioclase, biotites and hornblende. (a) The reverse zoning and compositional variation of a plagioclase crystal of the MME sample; The panel shows photomicrograph taken under cross–polarized light (left column), and An profile (right panel). The biotites from the granodiorite and associated MMEs are mainly plotted (b) in the re-equilibrated primary biotite field of the $10 * TiO_2$–FeO_{total}–MgO diagram (Nachit et al. 2005), (c) in the field of calc-alkaline magma of the MgO–FeO*–Al_2O_3 diagram (Abdel-Rahman 1994); (d) in the field of mantle-crust magma (after Zhou, 1986); TFeO indicates total iron as FeO; (e) the amphiboles from granodiorite and associated MMEs are mainly ferrohornblende to magnesiohornblende in composition (Leake et al., 1997); and (f) in the field of mantle-crust magma (Xie and Zhang 1990).

Figure 6. Position of the Mashhad granodiorite and enclosed MMEs on (a) TAS (Na_2O+K_2O vs. SiO_2) classification diagram (Middlemost 1994); (b) Quartz-Alkali feldspar–Plagioclase (QAP) normative classification diagram for Mashhad granodiorite and associated MMEs.; (c) K_2O vs. SiO_2 diagram with lines separating tholeiitic, calc-alkaline, high-K calc-alkaline and shoshonitic series (Peccerillo and Taylor 1976), and (d) A/NK (Al_2O_3/Na_2O+K_2O) vs. A/CNK ($Al_2O_3/CaO+Na_2O+K_2O$) plots (Shand 1943); (e) Discrimination diagram of Rb vs. Yb+Ta for the Mashhad granodiorite and associated MMEs (after Pearce et al. 1984). WPG: within-plate granitoids; VAG: volcanic arc granitoids; ORG: ocean ridge granitoids; syn-COLG: syncollisional granitoids. Pinkish and orange fields show granitoid rocks from Mashhad and Dehnow, respectively (Karimpour et al. 2010; Mirnejad et al. 2013). (f) Discrimination diagram of R2 (6Ca + 2Mg + Al) vs. R1 (4Si - 11(Na + K) - 2(Fe + Ti)) for the Mashhad granodiorite (Batchelor and Bodwen 1985).

Figure 7 (a) and (b) Chondrite-normalized REE patterns (Sun and McDonough 1989 for the Mashhad granodiorite and their MMEs, respectively; (c) and (d) Primitive-mantle normalized trace element patterns (Sun and McDonough 1989) for the Mashhad granodiorite and their MMEs, respectively.

Figure 8. Harker variation diagrams for major and some trace element compositions of the Mashhad granodiorite and their MMEs. The variation of samples from the MMEs and granitoids are continuous and display linear trends as might be expected if the enclaves formed by mixing. Published data of mafic end-member in the study area are shown, with filled square, come from Shafaii Moghadam et al. (2015).

Figure 9. Cathodoluminescence images for the MME in Mashhad granodiorite (sample GE-1)

Figure 10. Zircon U–Pb concordia diagram of the MMEs of the Mashhad granodiorite.

Figure 11. Initial $^{87}Sr/^{86}Sr$ vs. $\varepsilon Nd_{(t)}$ for the Mashhad granodiorite and MMEs. Data of Triassic granitoids and associated MMEs of the western Kunlun orogeny (Jiang et al. 2013), East Kunlun Orogen (Xia et al. 2015) and Tagong pluton in Songpan–Ganze terrane (Chen et al. 2017), from China, the eastern part of Paleo-Tethys suture zone.

Figure 12. (a) $(Fe_2O_3)_T$ vs. MgO and (b) $\varepsilon Nd_{(t)}$ vs. SiO_2 variations of host granitoids and MMEs from the Mashhad (Castro et al. 1990; Chappell 1996). (c) Geochemical correlation diagrams of Fe_2O_3/Al_2O_3 vs. Na_2O/CaO; (d) Rb (ppm) vs. Rb/Sr; data for gray and black symbols come from granitoid and associated MMEs from Buchan, China (Liu et al. 2013) (Langmuir et al. 1978; Blundy and Sparks 1992; Zhou 1994). Published data of mafic end-members in the study area come from Shafaii Moghadam et al. (2015) and are shown with filled squares.

Figure 13. (a) Th/Yb vs. Ta/Yb diagram (Pearce et al. 1990) for the Mashhad granodiorite and their MMEs; (b) The La/Yb vs. Sm/Nd diagram display negative correlation; (c) Nb/U vs. Nb diagram (Kepezhinskas et al. 1996). (d) Th/Nb vs. Ba/Th diagram with sediment melt and fluids trends from Ribeiro et al. (2013). N-MORB composition come from Sun and McDonough (1989). Subduction enrichment and mantle metasomatism are from Pearce et al. (1990). Nb enriched arc basalts (NEBs).

Figure 14. Schematic model explaining the development of magma mixing between mantle derived magmas and lower mafic crust-derived magmas within the magma chamber above a subduction zone, modified after Miller et al. (2007). Abbreviations: SCLM = sub-continental lithospheric mantle; PMMA= Pamir-Mashhad Magmatic Arc.

11. Table captions

Table 1. Representative EPMA analyses of plagioclases, biotites and amphiboles of the Mashhad granodiorite and its MMEs

Table 2. Major oxides (wt%) and trace element (ppm) contents of Mashhad granodiorite and its MMEs

Table 3. LA-ICP-MS U-Pb data on zircons and ages for The MMEs in Mashhad granodiorite

Table 4. Results of whole rock Sr-Nd isotope ratios of the Mashhad granodiorite and its MMEs

Figure 1

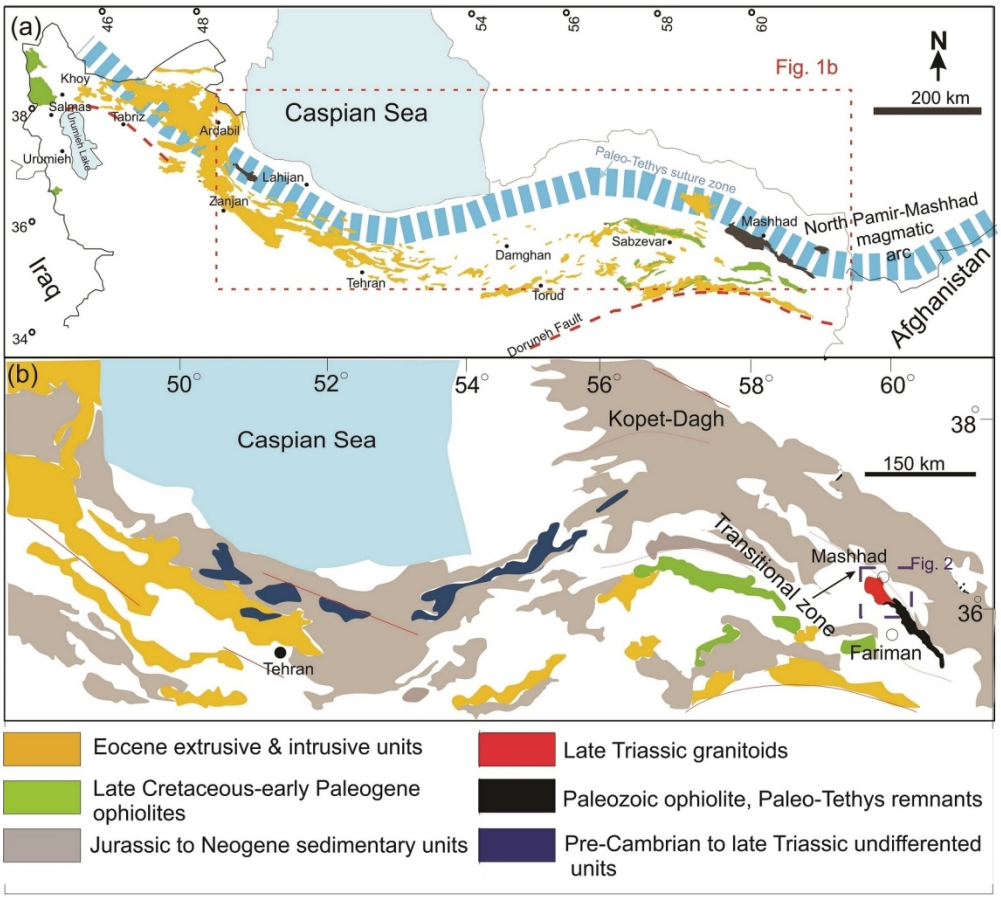

Figure 1. (a) the North Pamir–Mashhad arc passes south of Mashhad city and extends along the Alborz Mountain to southern Azerbaijan (modified after Natal'in and Şengör 2005), and (b) geological map of the Paleo-Tethys orogenic belt in northern Iran (after Zanchi et al. 2009).

151x144mm (300 x 300 DPI)

Figure 2

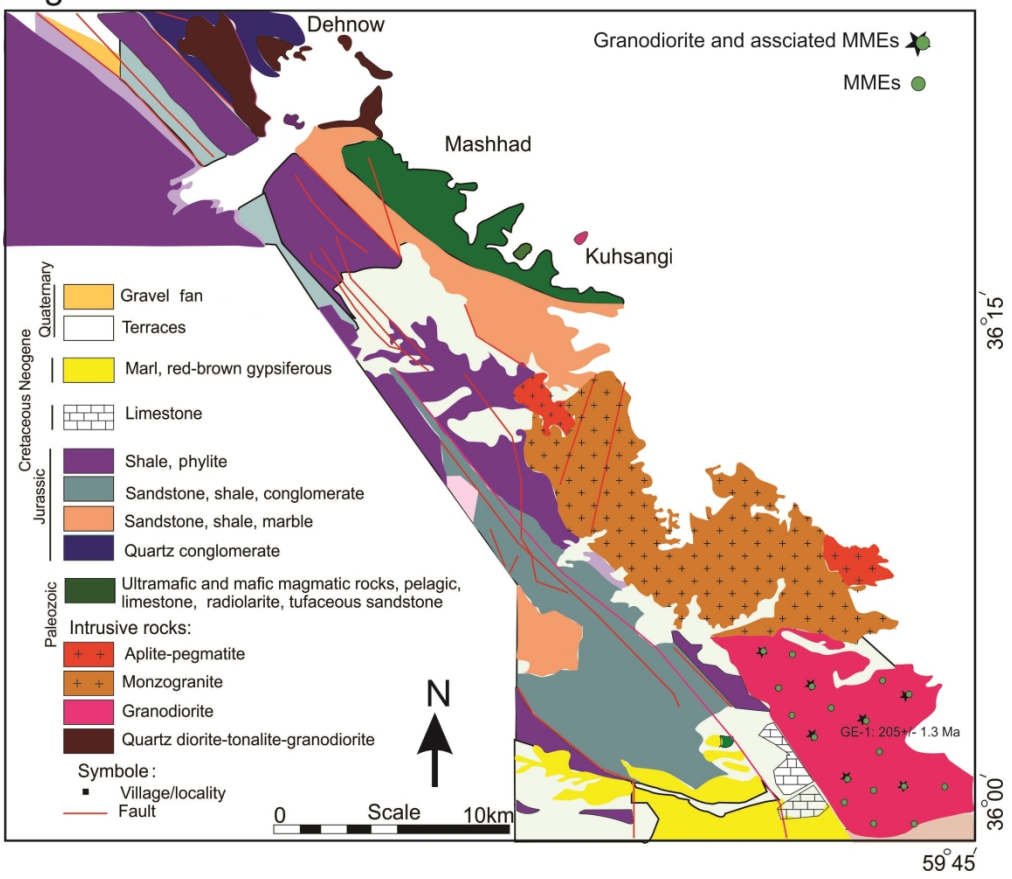

Figure 2. Geological map of the Mashhad batholith (modified after Mirnejad et al. 2013).

233x209mm (300 x 300 DPI)

Figure 3

Figure. 3. Relationships between MMEs and the Mashhad granodiorite host. (a) Cross cutting of rounded to ellipsoid MMEs and host granodiorite by late stage aplitic phase; (b) sigmoidal and elongated enclaves within Mashhad granodiorite, reflecting deformations during flow of the host magma; A view of (c) massive; (d) banded structures; (e) liner and (f) irregular boundaries patches enriched in fine-grained mafic material in the granodiorite host rocks; (g) Enclosing of feldspar megacrysts from the host by enclaves and (h) Enclosing of enclaves by feldspar megacrysts from the host.

67x57mm (300 x 300 DPI)

Figure 4

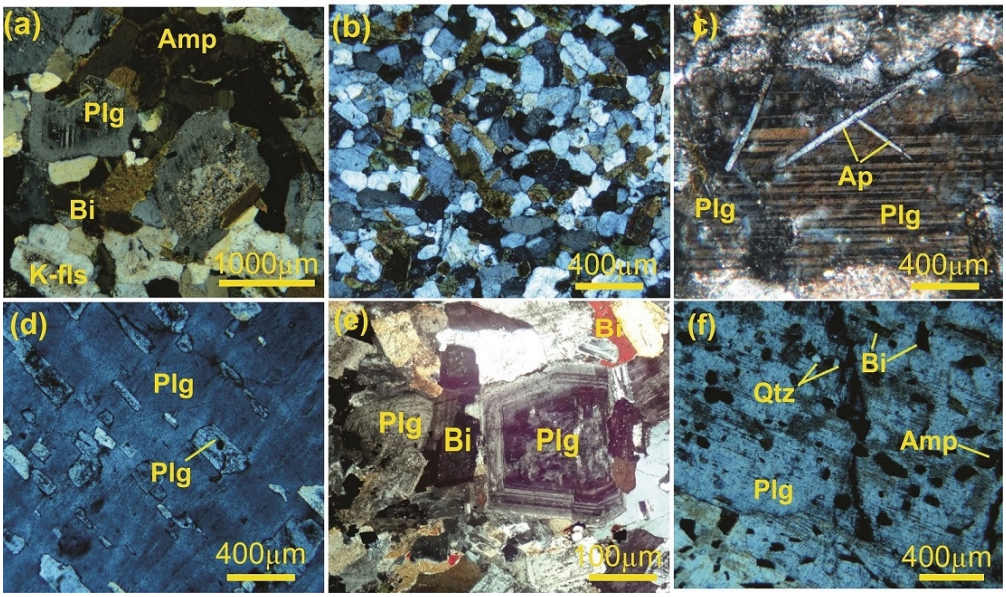

Figure 4. Thin section photographs (cross-polarised light) of representative MMEs from the Mashhad granodiorite. (a) Granular texture in the granodiorite with associated minerals; (b) Microgranular texture in the MMEs with associated minerals; (c) Acicular apatite in the plagioclase with resorption texture in the MMEs; (d) small lath-shaped plagioclase inclusions hosted by a large plagioclase in the MMEs; (e) oscillatory zoning in the plagioclase from MMEs; (f) inclusions of quartz, biotite and hornblende in plagioclase. Abbreviations: Amp = amphibole; Ap = Apatite; Bi = biotite; K-fls = K-feldspar; Plg = plagioclase; Qtz = quartz.

93x58mm (300 x 300 DPI)

Figure 5

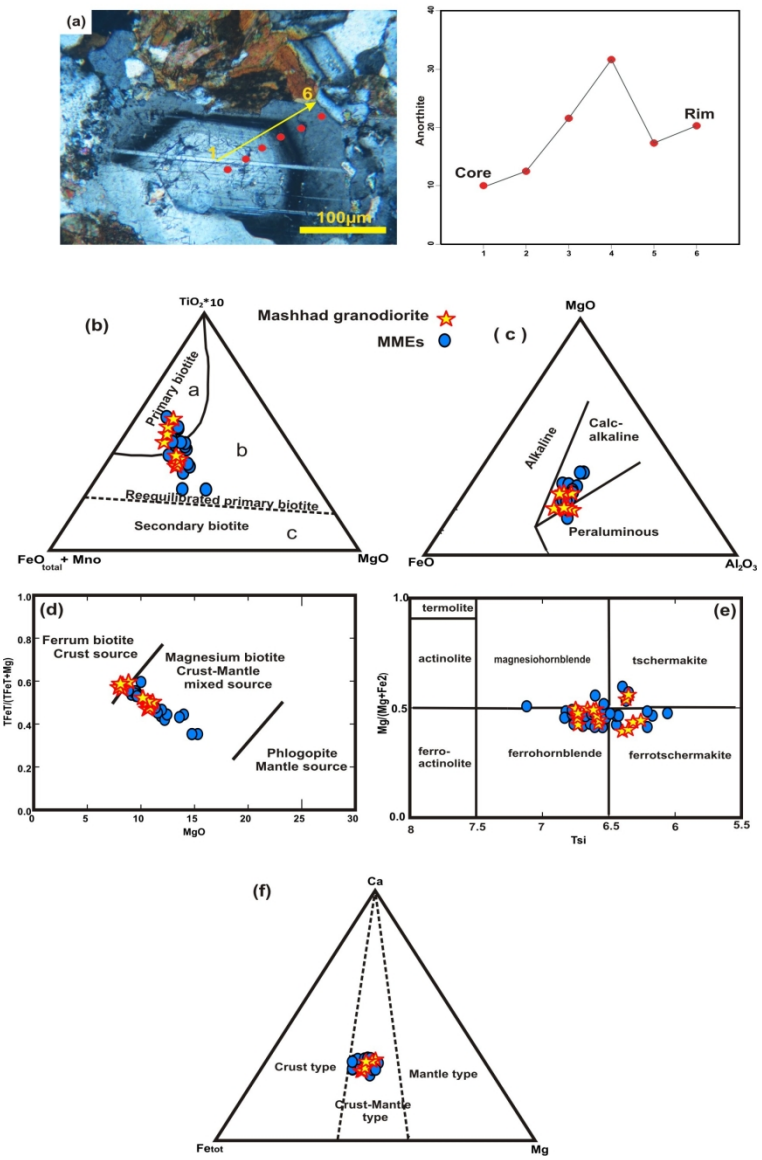

Figure 5. Compositional plots of plagioclase, biotites and hornblende. (a) The reverse zoning and compositional variation of a plagioclase crystal of the MME sample; The panel shows photomicrograph taken under cross–polarized light (left column), and An profile (right panel). The biotites from the granodiorite and associated MMEs are mainly plotted (b) in the re-equilibrated primary biotite field of the 10 ∗ TiO2–FeOtotal–MgO diagram (Nachit et al. 2005), (c) in the field of calc-alkaline magma of the MgO–FeO*–Al2O3 diagram (Abdel-Rahman 1994); (d) in the field of mantle-crust magma (after Zhou, 1986); TFeO indicates total iron as FeO; (e) the amphiboles from granodiorite and associated MMEs are mainly ferrohornblende to magnesiohornblende in composition (Leake et al., 1997); and (f) in the field of mantle-crust magma (Xie and Zhang 1990).

164x260mm (300 x 300 DPI)

Figure 6

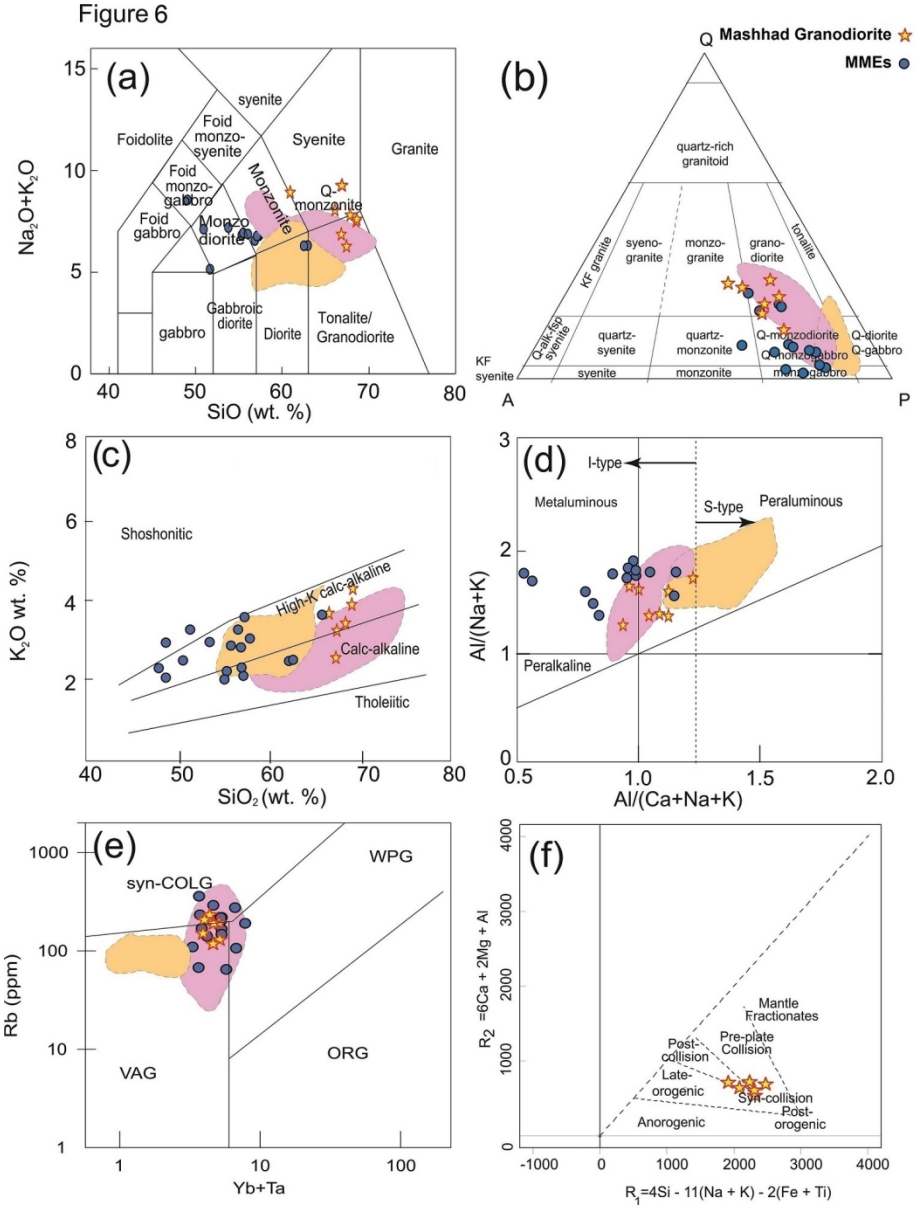

Figure 6. Position of the Mashhad granodiorite and enclosed MMEs on (a) TAS (Na2O+K2O vs. SiO2) classification diagram (Middlemost 1994); (b) Quartz-Alkali feldspar–Plagioclase (QAP) normative classification diagram for Mashhad granodiorite and associated MMEs.; (c) K2O vs. SiO2 diagram with lines separating tholeiitic, calc-alkaline, high-K calc-alkaline and shoshonitic series (Peccerillo and Taylor 1976), and (d) A/NK (Al2O3/Na2O+K2O) vs. A/CNK (Al2O3/CaO+Na2O+K2O) plots (Shand 1943); (e) Discrimination diagram of Rb vs. Yb+Ta for the Mashhad granodiorite and associated MMEs (after Pearce et al. 1984). WPG: within-plate granitoids; VAG: volcanic arc granitoids; ORG: ocean ridge granitoids; syn-COLG: syncollisional granitoids. Pinkish and orange fields show granitoid rocks from Mashhad and Dehnow, respectively (Karimpour et al. 2010; Mirnejad et al. 2013). (f) Discrimination diagram of R2 (6Ca + 2Mg + Al) vs. R1 (4Si - 11(Na + K) - 2(Fe + Ti)) for the Mashhad granodiorite (Batchelor and Bodwen 1985).

128x168mm (300 x 300 DPI)

Figure 7

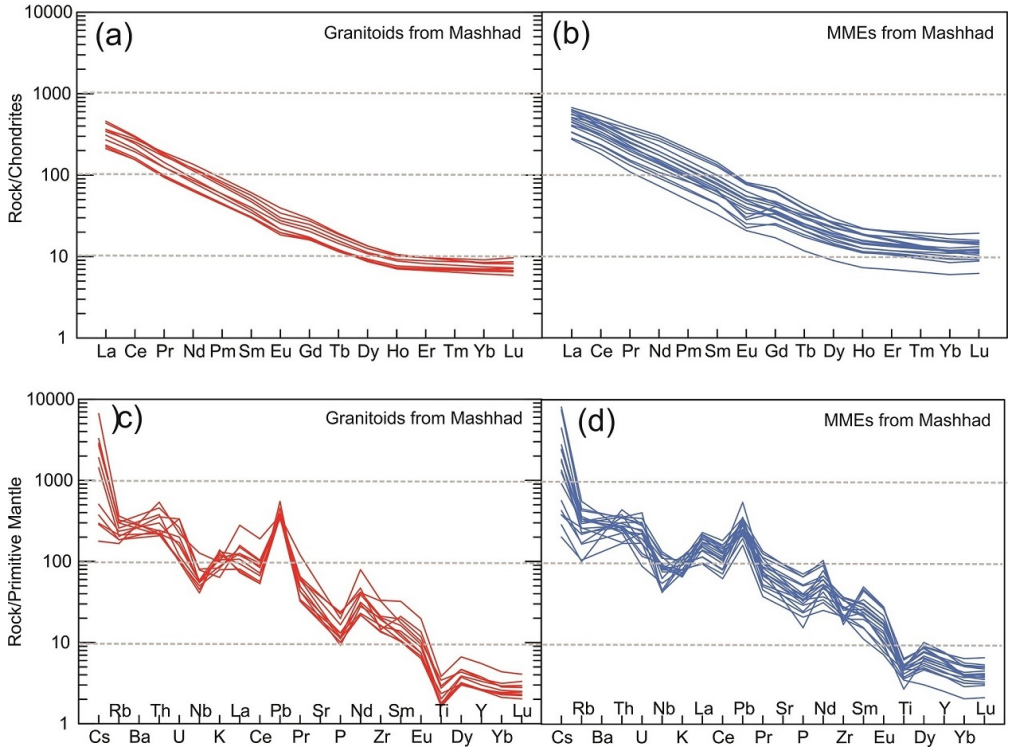

Figure 7 (a) and (b) Chondrite-normalized REE patterns (Sun and McDonough 1989 for the Mashhad granodiorite and their MMEs, respectively; (c) and (d) Primitive-mantle normalized trace element patterns (Sun and McDonough 1989) for the Mashhad granodiorite and their MMEs, respectively.

106x83mm (300 x 300 DPI)

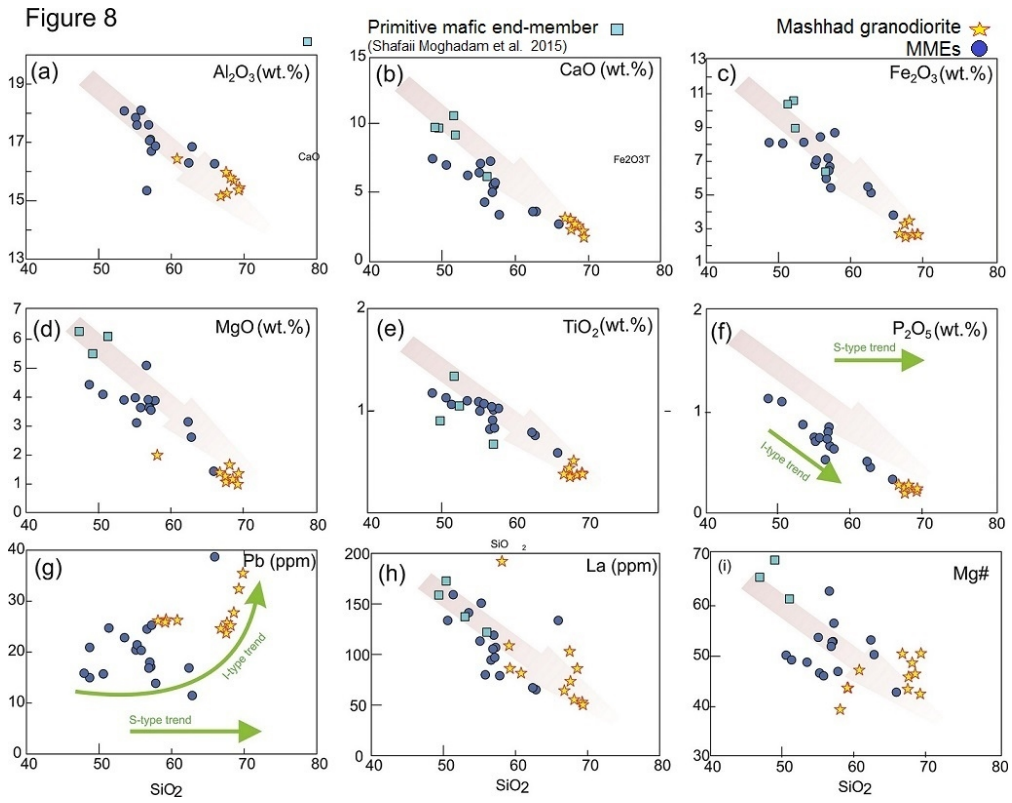

Figure 8. Harker variation diagrams for major and some trace element compositions of the Mashhad granodiorite and their MMEs. The variation of samples from the MMEs and granitoids are continuous and display linear trends as might be expected if the enclaves formed by mixing. Published data of mafic end-member in the study area are shown, with filled square, come from Shafaii Moghadam et al. (2015).

86x68mm (300 x 300 DPI)

Figure 9

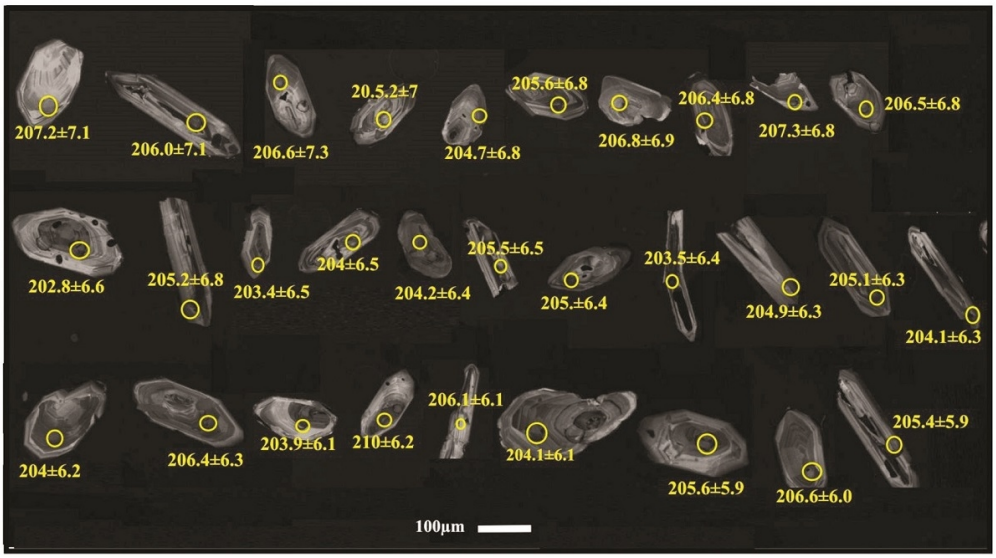

Figure 9. Cathodoluminescence images for the MME in Mashhad granodiorite (sample GE-1)

101x60mm (300 x 300 DPI)

Figure 10

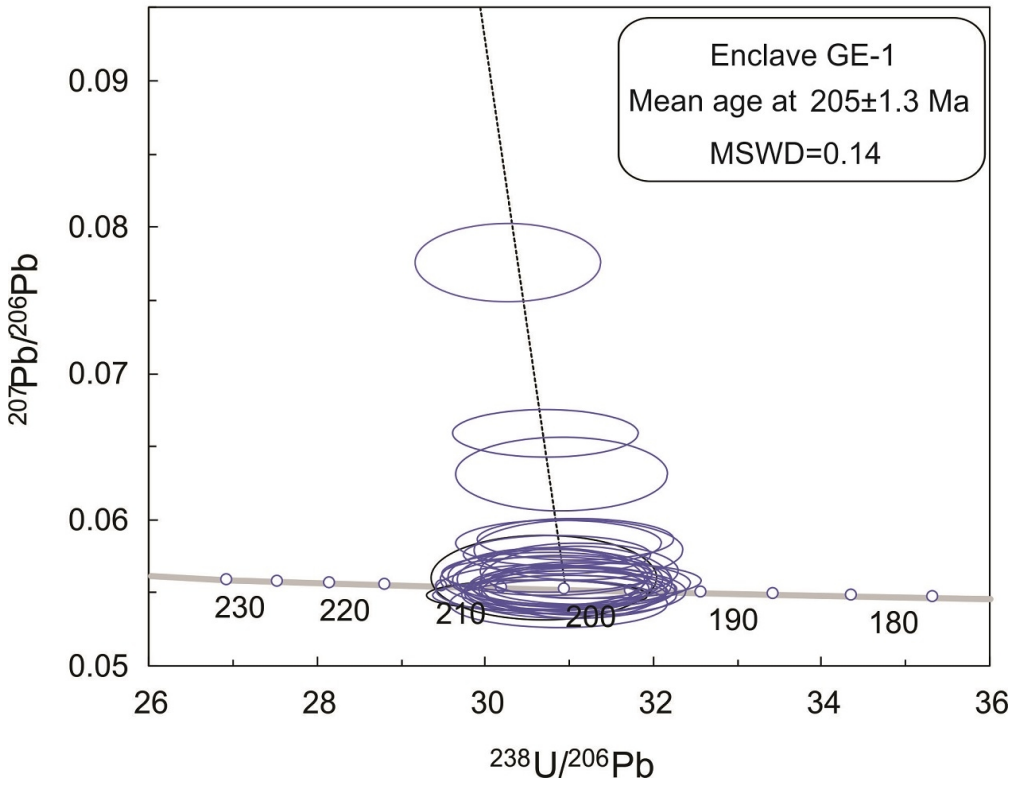

Figure 10. Zircon U–Pb concordia diagram of the MMEs of the Mashhad granodiorite.

106x88mm (300 x 300 DPI)

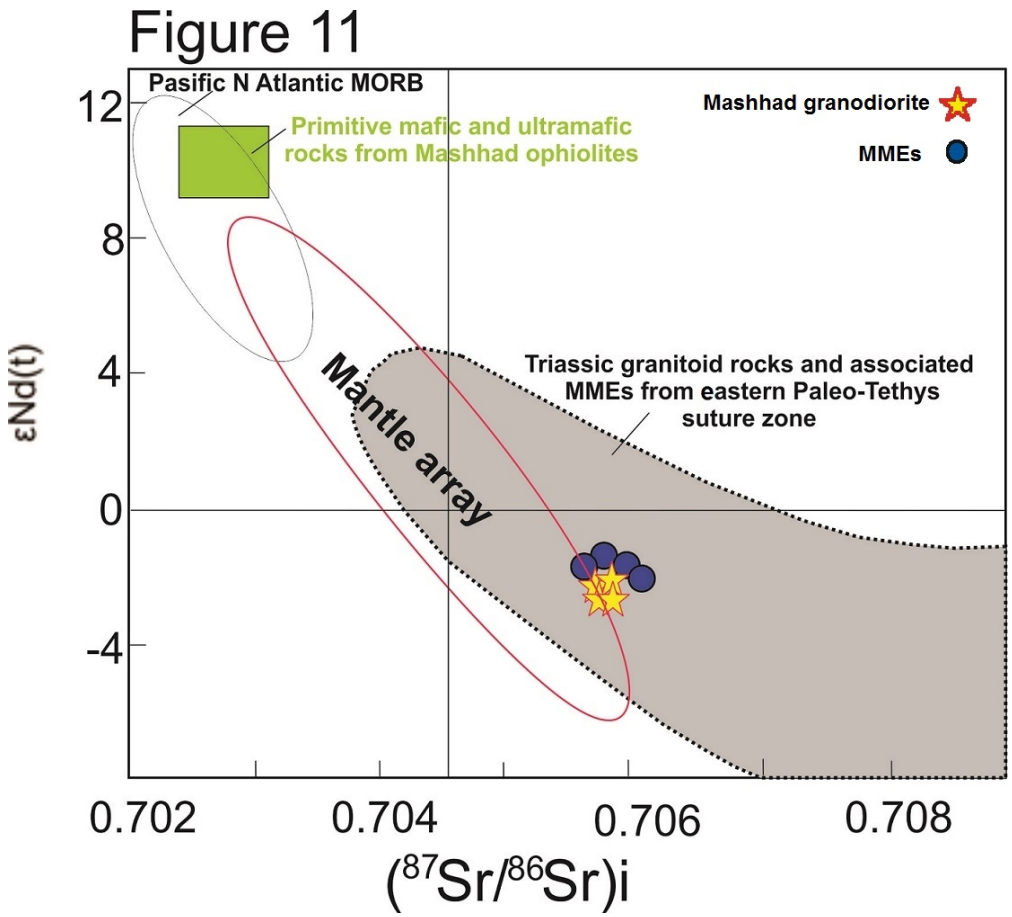

Figure 11. Initial 87Sr/86Sr vs. εNd(t) for the Mashhad granodiorite and MMEs. Data of Triassic granitoids and associated MMEs of the western Kunlun orogeny (Jiang et al. 2013), East Kunlun Orogen (Xia et al. 2015) and Tagong pluton in Songpan–Ganze terrane (Chen et al. 2017), from China, the eastern part of Paleo-Tethys suture zone.

94x85mm (300 x 300 DPI)

Figure 12

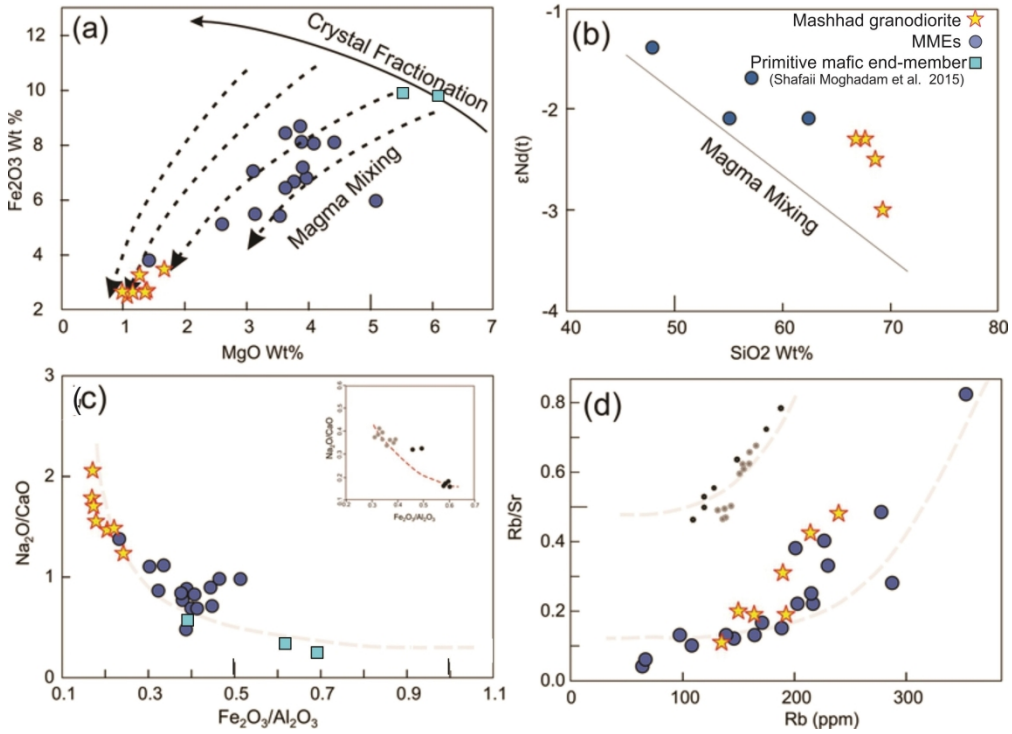

Figure 12. (a) (Fe2O3)T vs. MgO and (b) εNd(t) vs. SiO2 variations of host granitoids and MMEs from the Mashhad (Castro et al. 1990; Chappell 1996). (c) Geochemical correlation diagrams of Fe2O3/Al2O3 vs. Na2O/CaO; (d) Rb (ppm) vs. Rb/Sr; data for gray and black symbols come from granitoid and associated MMEs from Buchan, China (Liu et al. 2013) (Langmuir et al. 1978; Blundy and Sparks 1992; Zhou 1994). Published data of mafic end-members in the study area come from Shafaii Moghadam et al. (2015) and are shown with filled squares.

283x217mm (300 x 300 DPI)

Figure 13

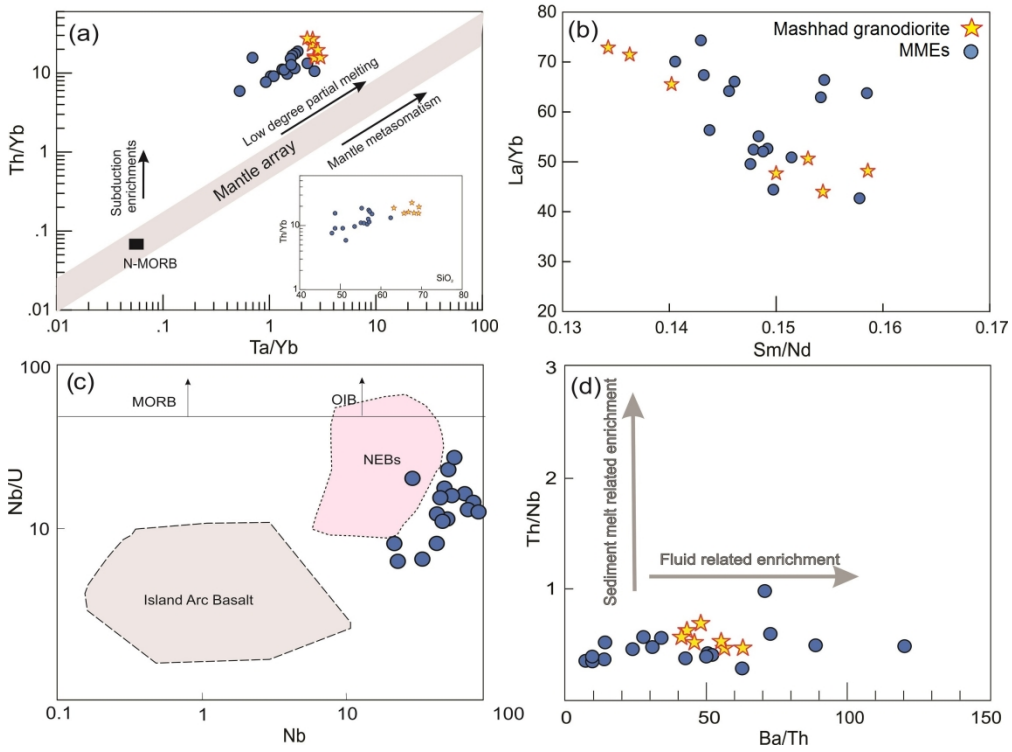

Figure 13. (a) Th/Yb vs. Ta/Yb diagram (Pearce et al. 1990) for the Mashhad granodiorite and their MMEs; (b) The La/Yb vs. Sm/Nd diagram display negative correlation; (c) Nb/U vs. Nb diagram (Kepezhinskas et al. 1996). (d) Th/Nb vs. Ba/Th diagram with sediment melt and fluids trends from Ribeiro et al. (2013). N-MORB composition come from Sun and McDonough (1989). Subduction enrichment and mantle metasomatism are from Pearce et al. (1990). Nb enriched arc basalts (NEBs).

222x172mm (300 x 300 DPI)

Figure 14

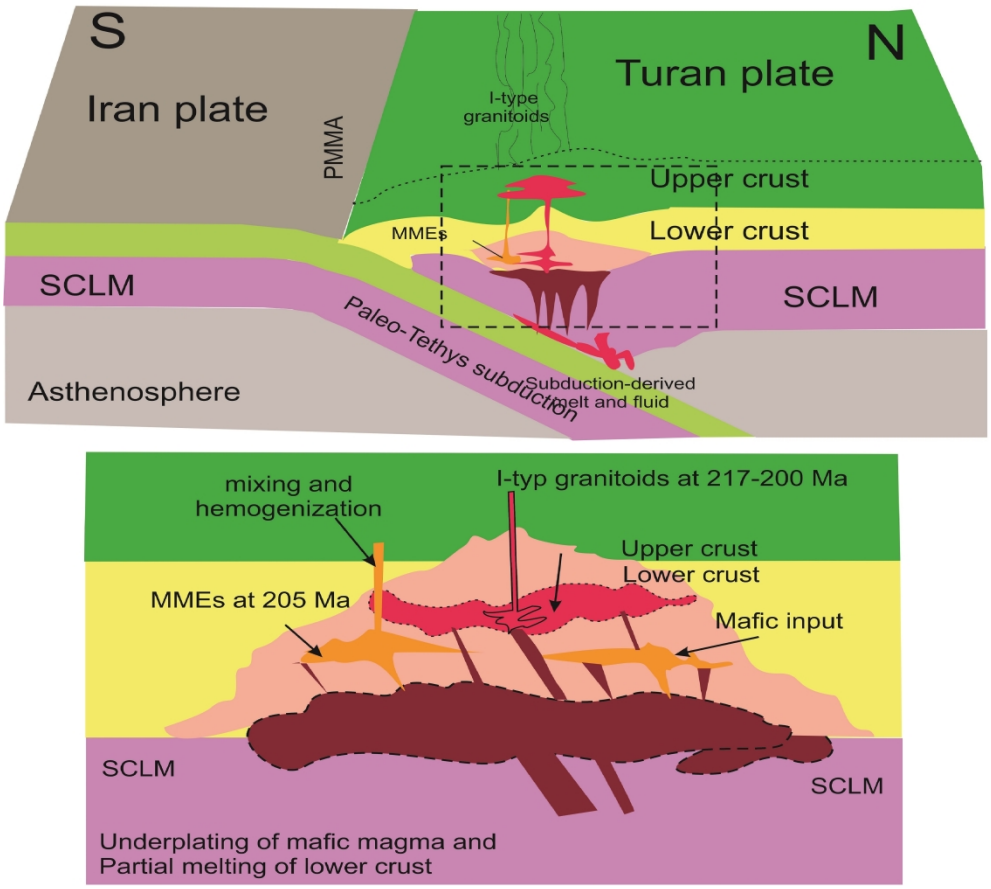

Figure 14. Schematic model explaining the development of magma mixing between mantle derived magmas and lower mafic crust-derived magmas within the magma chamber above a subduction zone, modified after Miller et al. (2007). Abbreviations: SCLM = sub-continental lithospheric mantle; PMMA= Pamir-Mashhad Magmatic Arc.

365x340mm (300 x 300 DPI)

Table 1 Representative EPMA analyses of biotites of the Mashhad granodiorite and its MMEs in Wt.% oxide.

	Granodiorite												MMEs	
Sample	**B1.5**	**B1.6**	**B1.10**	**B1.11**	**B3.70**	**B3.71**	**G11**	**G11.1**	**RE10.6**	**RE10.7**	**RE10.8**	**RE10.9**	**BE1.30**	**BE1.29**
SiO_2	37.05	36.77	37.30	36.71	36.26	36.62	38.04	38.23	36.91	36.18	36.75	36.23	37.01	36.84
TiO_2	2.02	2.03	1.86	1.95	2.72	3.08	1.68	1.74	3.52	3.36	3.65	3.42	2.41	2.34
Al_2O_3	14.57	14.78	14.65	15.10	15.41	14.69	14.64	14.65	16.69	16.39	16.80	17.49	15.19	15.12
FeO	19.65	19.19	19.21	18.87	21.35	21.42	17.81	17.55	19.94	20.41	20.53	19.44	17.95	18.13
MnO	0.61	0.59	0.71	0.76	0.56	0.61	0.61	0.70	0.56	0.58	0.60	0.53	0.39	0.41
MgO	10.51	10.19	10.97	10.97	8.67	8.72	10.89	10.89	8.38	8.42	8.21	7.87	11.96	11.90
CaO	0.01	0.02	0.02	0.03	0.01	0.01	0.05	0.05	0.02	0.04	0.06	0.03	0.02	0.02
Na_2O	0.02	0.07	0.10	0.11	0.05	0.09	0.02	0.07	0.05	0.05	0.07	0.07	0.05	0.04
K_2O	9.63	9.58	9.62	9.43	9.59	9.45	9.87	9.76	10.00	9.63	9.75	9.58	9.72	9.72
Total	94.13	93.28	94.51	94.00	94.69	94.76	93.67	93.70	96.13	95.12	96.47	94.73	94.75	94.58
Number of cations on the basis of 11 oxygens														
^{IV}Si	5.75	5.75	5.75	5.69	5.64	5.69	5.87	5.89	5.61	5.57	5.58	5.56	5.65	5.65
^{IV}Al	2.25	2.25	2.25	2.31	2.36	2.31	2.13	2.11	2.39	2.43	2.42	2.44	2.35	2.35
^{VI}Al	0.42	0.47	0.42	0.44	0.47	0.39	0.53	0.54	0.60	0.55	0.58	0.73	0.39	0.38
Ti	0.24	0.24	0.22	0.23	0.32	0.36	0.19	0.20	0.40	0.39	0.42	0.39	0.28	0.27
Fe	2.53	2.49	2.46	2.42	2.76	2.76	2.28	2.24	2.51	2.61	2.58	2.48	2.27	2.30
Mn	0.08	0.08	0.09	0.10	0.07	0.08	0.08	0.09	0.07	0.08	0.08	0.07	0.05	0.05
Mg	2.43	2.37	2.52	2.53	2.01	2.02	2.51	2.50	1.90	1.93	1.86	1.80	2.73	2.72
Ca	0.00	0.00	0.00	0.00	0.00	0.00	0.01	0.01	0.00	0.01	0.01	0.01	0.00	0.00
Na	0.01	0.02	0.03	0.03	0.02	0.03	0.01	0.02	0.01	0.01	0.02	0.02	0.01	0.01
K	1.91	1.91	1.89	1.86	1.90	1.88	1.94	1.92	1.94	1.89	1.89	1.88	1.89	1.90
Mg/(Mg+Fe)	0.49	0.49	0.50	0.51	0.42	0.42	0.52	0.53	0.43	0.42	0.42	0.42	0.54	0.54

Table 1 (continued) Representative EPMA analyses of biotites of the Mashhad granodiorite and its MMEs in Wt.% oxide.

	MMEs													
Sample	**GE10**	**GE11**	**KE4**	**KE5**	**KE6**	**KE17**	**KE18**	**KE25**	**KE26**	**KE22**	**KE23**	**RE11**	**RE13**	**RE12.2**
SiO_2	37.85	38.18	35.22	36.01	36.93	38.12	38.09	36.00	36.25	36.99	37.34	35.67	36.04	35.76
TiO_2	1.59	1.71	1.16	1.21	1.52	1.00	0.96	3.27	3.11	2.57	2.61	3.78	2.86	2.65
Al_2O_3	13.55	14.50	14.68	14.41	14.06	15.10	14.96	15.54	15.93	15.36	15.56	17.66	15.06	15.02
FeO	16.41	16.70	19.37	19.08	18.06	14.14	14.30	19.53	19.41	18.00	17.90	21.42	20.56	20.11
MnO	0.57	0.55	0.56	0.44	0.51	0.29	0.24	0.44	0.49	0.44	0.48	0.54	0.55	0.60
MgO	11.97	12.09	13.82	13.72	12.44	14.86	15.04	9.46	9.00	11.38	11.76	6.64	9.47	9.65
CaO	0.27	0.04	0.04	0.08	0.07	0.18	0.18	0.06	0.05	0.06	0.00	0.00	0.00	0.02
Na_2O	0.07	0.09	0.03	0.01	0.06	0.07	0.09	0.08	0.10	0.11	0.05	0.05	0.08	0.03
K_2O	8.16	9.21	6.82	7.04	9.27	8.81	8.90	9.65	9.96	9.67	9.79	9.72	9.93	9.48
Total	90.51	93.12	91.75	92.05	92.97	92.62	92.82	94.10	94.35	94.64	95.56	95.55	94.61	93.38
Number of cations on the basis of 11 oxygens														
^{IV}Si	5.96	5.87	5.54	5.63	5.75	5.80	5.79	5.60	5.62	5.66	5.65	5.49	5.61	5.62
^{IV}Al	2.04	2.13	2.46	2.37	2.25	2.20	2.21	2.40	2.38	2.34	2.35	2.51	2.39	2.38
^{VI}Al	0.47	0.50	0.26	0.28	0.34	0.51	0.47	0.44	0.53	0.43	0.43	0.70	0.38	0.41
Ti	0.19	0.20	0.14	0.14	0.18	0.11	0.11	0.38	0.36	0.30	0.30	0.44	0.34	0.31
Fe	2.14	2.13	2.53	2.47	2.33	1.78	1.80	2.52	2.49	2.28	2.24	2.74	2.66	2.62
Mn	0.08	0.07	0.07	0.06	0.07	0.04	0.03	0.06	0.06	0.06	0.06	0.07	0.07	0.08
Mg	2.81	2.77	3.24	3.20	2.89	3.37	3.41	2.19	2.08	2.59	2.65	1.53	2.20	2.26
Ca	0.05	0.01	0.01	0.01	0.01	0.03	0.03	0.01	0.01	0.01	0.00	0.00	0.00	0.00
Na	0.02	0.03	0.01	0.00	0.02	0.02	0.03	0.02	0.03	0.03	0.02	0.02	0.02	0.01
K	1.64	1.81	1.37	1.40	1.84	1.71	1.73	1.91	1.97	1.89	1.89	1.91	1.97	1.90
Mg/(Mg+Fe)	0.57	0.56	0.56	0.56	0.55	0.65	0.65	0.46	0.45	0.53	0.54	0.36	0.45	0.46

Table 1 (continued) Representative EPMA analyses of plagioclase of the MME in Wt.% oxide.

sample	**KE4.1**	**KE4.2**	**KE4.3**	**KE4.4**	**KE4.5**	**KE4.6**

SiO2	65.9	66.1	62.9	60.7	63.8	63.5
Al2O3	21.2	21.1	23.2	24.8	22.3	22.8
FeO	0.0	0.0	0.1	0.1	0.0	0.0
CaO	2.1	1.9	4.4	6.4	3.5	4.2
Na2O	10.1	7.2	8.7	7.6	9.2	8.9
K2O	0.2	0.1	0.2	0.1	0.1	0.1
TOTAL	99.6	96.5	99.3	99.6	99.0	99.5
An	10.0	12.5	21.6	31.6	17.3	20.3
Ab	88.8	86.7	77.5	67.8	82.0	78.9
Or	1.2	0.8	1.0	0.6	0.7	0.8
Number	1	2	3	4	5	6

Table 1 (continued) Representative EPMA analyses of amphiboles of the Mashhad granodiorite and its MMEs in Wt.% oxide.

	granodiorite													
sample	**G11.7**	**G11.8**	**G11.9**	**G11.10**	**K4.44**	**K4.45**	**K4.46**	**K4.51**	**K4.52**	**K17.28**	**K17.29**	**K17.33**	**K17.34**	**K17.35**
SiO2	45.43	45.22	44.94	43.25	40.99	41.26	42.23	44.03	42.92	43.82	44.04	42.94	43.73	43.97
TiO2	0.97	0.93	0.48	0.41	1.08	0.95	0.73	1.01	0.74	1.05	1.11	1.15	1.20	0.99
Al2O3	7.01	7.25	7.50	8.94	10.09	9.97	9.71	8.70	9.64	9.48	9.66	9.81	9.00	9.02
FeO	18.54	18.79	19.76	20.31	21.22	21.12	20.83	19.71	20.42	19.18	19.38	19.55	19.00	19.08
MnO	1.12	1.11	1.14	1.04	0.71	0.82	0.80	0.73	0.78	0.73	0.75	0.68	0.71	0.74
MgO	10.02	9.75	9.41	8.56	7.90	7.72	8.22	9.20	8.54	9.44	9.51	9.06	9.93	9.78
CaO	11.46	11.21	11.21	11.38	11.13	10.82	10.82	11.14	11.29	11.48	11.36	11.23	11.63	11.44
Na2O	1.53	1.45	1.20	1.44	1.54	1.61	1.52	1.54	1.59	1.56	1.55	1.55	1.60	1.54
K2O	0.96	1.01	0.94	1.28	1.62	1.61	1.45	1.27	1.38	1.28	1.22	1.44	1.26	1.23
Number of cations on the basis of 23 oxygens														
Si	6.75	6.57	6.76	6.56	6.75	6.25	6.32	6.73	6.75	6.59	6.59	6.57	6.66	6.37
Al (iv)	1.25	1.43	1.24	1.44	1.25	1.75	1.68	1.27	1.25	1.41	1.41	1.43	1.34	1.63
Al (vi)	0.35	0.32	0.37	0.35	0.58	0.36	0.37	0.50	0.48	0.59	0.52	0.49	0.60	0.37
Ti	0.10	0.11	0.11	0.07	0.06	0.27	0.19	0.06	0.09	0.11	0.13	0.10	0.06	0.11
Cr	0.00	0.00	0.00	0.00	0.00	0.00	0.00	0.00	0.01	0.00	0.01	0.00	0.00	0.00
Fe	2.42	2.55	2.48	2.52	2.35	2.52	2.53	2.63	2.56	2.34	2.31	2.32	2.35	1.80
Mn	0.09	0.11	0.10	0.11	0.05	0.06	0.06	0.06	0.06	0.09	0.09	0.09	0.08	0.08
Mg	2.26	2.00	2.20	2.08	2.30	1.96	1.97	2.04	2.11	2.17	2.18	2.11	2.21	2.05
Ca	1.89	1.87	1.86	1.88	1.92	1.88	1.90	1.93	1.89	1.90	1.96	1.92	1.95	1.88
Na	0.45	0.49	0.46	0.45	0.40	0.47	0.46	0.42	0.43	0.34	0.35	0.34	0.33	0.40
K	0.25	0.27	0.25	0.27	0.27	0.36	0.36	0.25	0.25	0.28	0.26	0.23	0.25	0.28
Mg#	48.33	43.97	47.06	45.26	49.44	43.72	43.85	43.75	45.23	48.12	48.56	47.61	48.47	53.25

Table 1 (continued) Representative EPMA analyses of amphiboles of the Mashhad granodiorite and its MMEs in Wt.% oxide.

	MMEs												
sample	**BE1.26**	**BE1.27**	**BE1.28**	**BE1.31**	**BE1.32**	**BE4.12**	**BE4.13**	**BE4.14**	**GE10.52**	**GE10.59**	**GE10.60**	**GE10.61**	**KE4.27**	**KE4.28**
SiO2	41.63	41.84	41.51	41.81	42.35	42.71	42.50	42.54	43.66	44.62	43.23	43.47	42.39	42.25
TiO2	0.99	1.23	0.93	0.93	0.80	1.30	1.36	0.81	0.60	0.54	0.60	0.55	1.23	0.96
Al2O3	11.12	10.90	11.02	11.06	10.55	9.63	9.77	9.96	9.03	8.20	9.42	9.06	10.03	10.28
FeO	18.60	18.53	18.94	18.71	18.20	19.41	20.40	21.18	18.81	18.15	18.92	18.60	18.82	19.05
MnO	0.61	0.61	0.56	0.60	0.53	0.65	0.73	0.67	0.95	0.96	0.92	0.90	0.68	0.68
MgO	9.00	9.03	9.25	9.24	9.37	9.13	8.25	8.12	9.67	10.10	9.26	9.57	9.72	9.16
CaO	11.50	11.47	11.52	11.59	11.46	11.24	11.34	11.02	11.56	11.56	11.32	11.45	11.37	11.22
Na2O	1.36	1.44	1.49	1.43	1.49	1.61	1.41	1.39	1.44	1.38	1.48	1.49	1.65	1.73
K2O	1.42	1.41	1.43	1.34	1.32	1.21	1.26	1.18	1.30	1.07	1.29	1.25	1.50	1.52
Number of cations on the basis of 23 oxygens														
Si	6.37	6.35	6.40	6.49	6.44	6.59	6.76	6.60	6.70	6.57	6.55	6.59	6.54	7.11
Al (iv)	1.63	1.65	1.60	1.51	1.56	1.41	1.24	1.40	1.30	1.43	1.45	1.41	1.46	0.89
Al (vi)	0.37	0.34	0.39	0.25	0.22	0.62	0.69	0.67	0.33	0.40	0.43	0.40	0.32	0.37
Ti	0.11	0.11	0.11	0.09	0.10	0.09	0.17	0.17	0.05	0.14	0.11	0.13	0.08	0.10
Cr	0.00	0.00	0.00	0.00	0.00	0.00	0.00	0.00	0.01	0.00	0.00	0.00	0.00	0.00
Fe	1.80	1.64	1.47	2.19	2.51	2.41	2.55	2.56	2.63	2.44	2.47	2.41	2.70	2.41
Mn	0.08	0.07	0.08	0.11	0.10	0.08	0.07	0.08	0.14	0.09	0.09	0.09	0.10	0.11
Mg	2.05	2.11	2.11	1.91	1.86	2.21	1.90	1.82	1.98	2.25	2.12	2.23	1.90	2.40
Ca	1.88	1.89	1.90	1.87	1.83	1.66	1.92	1.87	1.89	1.89	1.86	1.88	1.80	1.91
Na	0.40	0.44	0.42	0.46	0.44	0.24	0.29	0.39	0.43	0.50	0.52	0.49	0.46	0.40
K	0.28	0.28	0.26	0.24	0.24	0.18	0.18	0.18	0.25	0.30	0.30	0.27	0.29	0.20
Mg#	53.25	56.27	58.85	46.64	42.55	47.80	42.80	41.62	42.90	47.93	46.16	48.07	41.29	49.94

Table 1 (continued) Representative EPMA analyses of amphiboles of the Mashhad granodiorite and its MMEs in Wt.% oxid

MMEs												
K17.36	**sample**	**KE4.30**	**KE4.37**	**KE4.38**	**KE4.39**	**KE15.58**	**KE15.62**	**KE15.75**	**KE17.4**	**KE17.5**	**KE17.9**	**KE17.10**
43.08	**SiO2**	43.57	42.41	43.62	42.34	42.83	43.54	47.06	44.645	42.94	51.11	41.48
0.89	**TiO2**	0.89	0.98	0.94	0.62	1.26	0.54	0.25	0.384	0.73	0.10	0.56
10.00	**Al2O3**	8.75	9.57	8.81	9.77	10.10	10.05	6.66	9.960	11.15	4.22	11.62
19.56	**FeO**	18.69	19.68	19.13	19.41	18.64	18.17	18.25	15.943	16.64	13.98	18.75
0.72	**MnO**	0.72	0.83	0.78	0.81	0.44	0.39	0.46	0.316	0.27	0.38	0.37
9.11	**MgO**	9.80	8.66	9.54	9.00	9.24	9.96	10.79	11.240	10.63	13.84	9.14
11.37	**CaO**	11.40	11.25	11.17	11.30	11.42	11.59	11.97	11.753	11.73	12.65	11.77
1.50	**Na2O**	1.498	1.642	1.53	1.49	1.36	1.33	0.96	1.485	1.583	0.623	1.440
1.30	**K2O**	1.286	1.389	1.28	1.38	1.41	1.37	0.73	1.233	1.495	0.384	1.671
	Number of cations on the basis of 23 oxygens											
6.35	**Si**	6.651	6.239	6.21	6.64	6.06	6.21	6.43	6.171	6.538	6.790	6.825
1.65	**Al (iv)**	1.349	1.761	1.79	1.36	1.94	1.79	1.57	1.829	1.462	1.210	1.175
0.34	**Al (vi)**	0.413	0.366	0.34	0.48	0.39	0.65	0.55	0.200	0.499	0.521	0.590
0.11	**Ti**	0.086	0.223	0.28	0.15	0.21	0.26	0.06	0.131	0.089	0.122	0.130
0.00	**Cr**	0.000	0.000	0.00	0.00	0.00	0.00	0.00	0.000	0.000	0.000	0.000
1.64	**Fe**	2.646	2.514	2.56	2.42	2.28	2.29	2.43	2.391	2.236	2.485	2.511
0.07	**Mn**	0.102	0.060	0.06	0.06	0.04	0.04	0.05	0.044	0.048	0.095	0.098
2.11	**Mg**	1.973	1.911	1.80	2.13	2.01	2.09	2.11	2.010	2.321	2.182	2.197
1.89	**Ca**	1.875	1.881	1.92	1.90	1.95	1.93	1.95	1.954	1.927	1.905	1.886
0.44	**Na**	0.479	0.507	0.47	0.41	0.45	0.47	0.43	0.412	0.445	0.470	0.466
0.28	**K**	0.272	0.374	0.39	0.28	0.41	0.40	0.33	0.345	0.286	0.253	0.242
56.27	**Mg#**	42.72	43.18	41.35	46.90	46.79	47.70	46.48	45.66	50.93	46.75	46.66

Table 1 (continued) Representative EPMA analyses of amphiboles of the Mashhad granodiorite and its MMEs in Wt.% oxid

MMEs								
KE4.29	**sample**	**KE17.14**	**KE17.15**	**KE17.16**	**KE17.20**	**KE25.49**	**KE25.50**	**KE25.51**	**KE25.52**
42.54	**SiO2**	51.48	53.10	39.82	42.19	42.54	42.53	42.43	42.96
1.13	**TiO2**	0.36	0.00	1.13	0.76	0.97	1.08	0.85	0.50
9.91	**Al2O3**	2.68	0.98	11.11	10.74	10.91	10.57	10.50	10.67
18.59	**FeO**	10.43	9.37	18.45	17.25	18.06	17.82	17.89	18.14
0.68	**MnO**	0.36	0.40	0.33	0.36	0.69	0.70	0.68	0.58
9.65	**MgO**	11.07	12.14	8.70	10.05	9.39	9.43	9.12	9.57
11.33	**CaO**	22.75	23.34	11.77	11.61	11.42	11.83	11.58	11.74
1.62	**Na2O**	0.67	0.56	1.37	1.48	1.12	1.15	1.12	1.08
1.38	**K2O**	0.031	0.050	1.74	1.45	1.43	1.31	1.18	1.27
	Number of cations on the basis of 23 oxygens								
6.82	**Si**	6.654	6.777	6.81	6.68	6.60	6.44	6.53	6.52
1.18	**Al (iv)**	1.346	1.223	1.19	1.32	1.40	1.56	1.47	1.48
0.41	**Al (vi)**	0.446	0.421	0.46	0.50	0.47	0.26	0.30	0.18
0.12	**Ti**	0.134	0.140	0.12	0.10	0.06	0.07	0.06	0.10
0.00	**Cr**	0.006	0.000	0.00	0.00	0.00	0.00	0.00	0.00
2.55	**Fe**	2.534	2.462	2.47	2.53	1.51	2.21	1.97	2.34
0.10	**Mn**	0.089	0.093	0.10	0.09	0.11	0.10	0.09	0.11
2.13	**Mg**	2.093	2.294	2.26	2.11	1.89	1.91	1.88	1.90
1.85	**Ca**	1.864	1.931	1.90	1.89	1.86	1.84	1.88	1.84
0.46	**Na**	0.465	0.480	0.46	0.45	0.41	0.41	0.40	0.40
0.25	**K**	0.284	0.249	0.24	0.26	0.24	0.26	0.24	0.24
45.43	**Mg#**	45.24	48.24	47.76	45.38	55.61	46.37	48.80	44.75

Table 2 **Major oxides (wt%) and trace element (ppm) contents of Mashhad granodiorite and its MMEs**

Rock Type	MMEs													
Sample No.	BE1	KE24	KE26	KE27	KE4	BE3	GE1	GE10	GE4	RE11	RE12	RE5	RE7	RE1
SiO_2	48.75	56.65	55.12	53.55	55.30	50.64	57.16	57.03	57.29	65.98	55.85	62.88	57.85	62.44
Al_2O_3	18.18	15.34	17.84	18.07	17.58	19.42	17.09	17.05	16.69	16.26	18.09	16.84	16.87	16.29
$Fe_2O_3^T$	8.09	5.96	6.79	8.11	7.04	8.05	6.66	6.43	5.41	3.79	8.43	5.11	8.68	5.48
MgO	4.42	5.09	3.97	3.89	3.11	4.09	3.77	3.63	3.54	1.43	3.63	2.61	3.87	3.14
CaO	7.40	7.22	6.39	6.19	7.05	6.95	5.47	5.49	5.67	2.65	4.24	3.56	3.32	3.56
Na_2O	6.61	3.43	4.91	4.38	4.84	4.75	4.81	4.59	4.88	3.63	4.14	3.92	3.24	3.96
K_2O	2.00	3.18	1.97	2.87	2.14	2.42	2.04	2.24	3.47	3.53	2.78	2.45	2.97	2.39
TiO_2	1.17	0.82	1.09	1.10	0.99	1.12	1.01	0.91	0.83	0.59	1.07	0.76	1.02	0.79
MnO	0.18	0.14	0.14	0.20	0.24	0.17	0.21	0.22	0.13	0.10	0.22	0.13	0.22	0.15
P_2O_5	1.13	0.53	0.75	0.88	0.71	1.10	0.85	0.80	0.67	0.34	0.75	0.46	0.64	0.51
H_2O+	0.27	0.53	-	0.00	0.19	0.30	0.09	0.32	0.53	0.07	0.01	0.22	0.01	-
H_2O-	0.94	0.54	0.63	0.78	0.28	0.61	0.69	0.42	0.42	0.57	0.59	0.73	0.80	0.69
Total	99.39	99.63	99.74	100.23	99.72	99.86	99.98	99.33	99.82	99.06	99.88	99.77	99.58	99.43
V	136	93.5	118	119	174	113	122	120	84.1	34.2	126.5	72.9	112.0	90.7
Cr	4.26	93.97	3.77	8.68	1.74	1.70	9.38	6.67	21.2	4.04	1.68	12.14	19.15	13.66
Co	29.9	35.2	28.5	25.1	39.0	24.9	31.1	30.2	26.9	35.8	28.3	30.1	28.5	28.6
Ni	4.82	49.75	8.49	7.02	7.54	3.91	11.2	10.9	20.2	2.09	2.40	8.47	15.0	13.7
Rb	165	105	203	189	64.1	146	217	288	139	201	272	230	356	216
Sr	1290	786	923	1241	1609	1188	992	1029	1084	526	553	704	413	515
Y	29.2	19.5	23.9	33.7	25.3	27.8	22.3	20.2	17.8	23.9	34.9	11.5	17.7	17.5
Zr	400	222	379	412	300	374	232	285	303	304	315	237	250	221
Nb	60.0	79.0	62.4	88.7	82.4	63.2	66.3	54.0	44.5	58.5	95.1	38.9	68.6	57.0
Ba	1195	1192	1220	1313	1200	1140	354	1031	1855	942	298	317	258	247
La	148	94	113	141	150	133	97	119	107	133	79.6	64.9	78.7	66.9
Ce	270	169	206	257	287	240	193	223	194	230	144	111	141	126
Pr	27.0	17.0	20.8	26.4	30.6	24.1	20.5	23.4	19.5	21.6	14.5	10.4	13.8	12.5
Nd	91.1	57.5	71.7	90.8	106.3	81.8	71.8	81.8	66.1	68.4	50.3	34.2	46.3	42.7
Sm	13.1	8.71	10.7	13.6	15.2	12.1	10.6	11.5	9.47	10.0	9.66	4.98	6.87	6.74
Eu	3.19	2.20	2.60	3.16	3.65	2.92	2.60	2.82	2.34	1.63	1.74	1.20	1.30	1.46
Tb	1.14	0.77	0.94	1.27	1.13	1.08	0.88	0.88	0.77	0.93	1.21	0.436	0.689	0.647
Gd	8.98	6.03	7.51	9.70	9.34	8.49	7.12	7.33	6.18	6.99	8.39	3.47	5.20	4.97
Dy	5.81	3.91	4.86	6.60	5.11	5.63	4.41	4.14	3.66	4.66	6.72	2.26	3.52	3.44
Ho	1.04	0.714	0.889	1.23	0.869	1.04	0.799	0.716	0.649	0.826	1.23	0.411	0.644	0.625
Er	2.89	1.94	2.37	3.38	2.33	2.88	2.17	1.95	1.82	2.25	3.25	1.14	1.72	1.75
Yb	2.63	1.85	2.15	3.18	2.02	2.54	1.96	1.70	1.59	2.02	2.80	1.01	1.43	1.57
Lu	0.381	0.285	0.334	0.489	0.300	0.370	0.299	0.244	0.231	0.296	0.399	0.157	0.223	0.232
Hf	8.14	5.17	8.37	9.17	5.98	8.09	5.35	6.14	6.46	6.51	7.12	5.47	5.81	5.17
Ta	2.73	4.95	2.86	4.71	3.76	2.81	3.42	2.98	2.63	3.30	3.88	2.74	2.28	3.60
Pb	14.9	24.5	20.4	22.8	21.4	15.7	17.1	18.0	25.2	38.6	20.3	11.4	13.8	16.8
Th	23.7	19.3	23.6	30.6	37.5	22.9	22.2	29.5	26.1	32.5	30.4	19.5	21.5	20.6
U	3.48	4.67	5.22	5.91	6.06	2.68	4.03	6.32	6.46	3.53	7.23	1.86	2.47	4.62
∑REE	575	365	444	557	614	516	413	478	413	483	324	235	301	270
(La/Yb)N	70.31	24.35	41.39	44.60	32.19	44.85	25.90	41.21	42.53	57.11	26.83	15.77	52.74	31.84
Eu/Eu*	0.90	0.93	0.89	0.84	0.94	0.88	0.92	0.94	0.93	0.60	0.59	0.88	0.66	0.77
Ba/La	8.10	12.65	10.80	9.31	7.97	8.55	3.66	8.68	17.39	7.07	3.74	4.87	3.28	3.69
Nb/La	0.41	0.84	0.55	0.63	0.55	0.47	0.69	0.45	0.42	0.44	1.19	0.60	0.87	0.85
Ba/Zr	2.98	5.38	3.22	3.19	4.00	3.05	1.53	3.62	6.13	3.10	0.94	1.34	1.03	1.12
Rb/Sr	0.13	0.13	0.22	0.15	0.04	0.12	0.22	0.28	0.13	0.38	0.49	0.33	0.86	0.42
Nb/Ce	0.22	0.47	0.30	0.35	0.29	0.26	0.34	0.24	0.23	0.25	0.66	0.35	0.49	0.45
Th/Ta	8.71	3.90	8.25	6.50	9.98	8.12	6.50	9.92	9.90	9.86	7.83	7.12	9.43	5.73

D.L. = Detectin Limit; * Dilution Factor of 2000; ** Dilution Factor of 4000

Table 2 (continued)

Rock Type	MMEs				Granodiorite							Standard	
Sample No.	KE25	KE15	KE16E	KE17E	B1	G11	G3	KE17H	R2	R7	RE10	BHVO-1	D.L.*
SiO_2	56.91	51.40	47.98	48.75	67.63	67.53	68.57	66.78	69.26	68.14	69.36	50.32	5.00
Al_2O_3	17.59	11.66	12.98	13.51	15.25	15.97	15.68	15.16	15.36	15.78	15.45	13.41	5.00
$Fe_2O_3^T$	7.18	11.89	12.12	10.35	2.51	3.27	2.65	2.71	2.66	3.48	2.64	12.14	5.00
MgO	3.91	5.81	5.73	6.01	1.07	1.27	1.16	1.39	0.99	1.67	1.36	7.09	3.00
CaO	4.96	11.07	12.54	11.69	2.26	3.02	2.54	3.11	2.14	2.67	1.70	11.25	3.00
Na_2O	4.08	2.02	2.83	2.59	6.18	4.43	4.54	4.54	3.77	3.96	3.49	2.37	2.50
K_2O	2.75	3.18	2.23	2.85	3.16	2.50	3.34	3.58	3.79	2.38	4.18	0.55	2.50
TiO_2	1.04	1.06	1.40	1.34	0.35	0.44	0.37	0.38	0.39	0.51	0.38	2.74	2.50
MnO	0.17	0.27	0.20	0.22	0.06	0.10	0.08	0.09	0.08	0.10	0.08	0.17	2.50
P_2O_5	0.74	1.42	1.43	1.55	0.20	0.25	0.24	0.29	0.22	0.28	0.25	0.28	2.50
H_2O+	0.01	0.22	0.08	0.06	0.24	0.18	-0.07	0.27	0.27	0.02	0.04		
H_2O-	0.00	0.49	0.59	0.66	0.62	0.23	0.38	0.53	0.37	0.61	0.64		
Total	99.47	100.7	100.3	99.85	99.71	99.37	99.66	99.03	99.45	99.72	99.69		D.L.**
V	105	292	304	237	30.4	44.2	35.8	43.0	28.0	39.4	25.0	332.05	0.12
Cr	7.61	0.83	3.51	2.41	2.41	2.78	4.31	5.66	5.03	6.33	4.77	292.50	0.20
Co	39.4	57.1	49.6	44.3	62.4	51.9	59.4	37.8	40.2	49.0	35.0	44.11	0.01
Ni	11.7	7.59	8.02	15.6	1.51	2.18	2.71	3.81	2.54	4.02	2.68	118.02	0.08
Rb	215	168	66.9	108	150	192	164	117	231	190	207	9.65	0.03
Sr	868	950	1116	1054	749	1020	856	859	468	608	474	416.20	0.37
Y	22.1	35.1	26.9	28.3	11.7	15.2	11.9	13.6	12.1	11.7	11.7	25.02	0.02
Zr	387	207	190	227	224	229	214	178	155	183	151	184.04	0.94
Nb	58.4	31.9	30.4	29.9	40.7	57.5	38.9	39.9	32.2	35.7	29.2	18.09	0.01
Ba	645	1712	1240	2097	1099	1029	943	1124	793	746	971	129.28	0.28
La	105	159	121	130	73.4	102.9	86.0	64.3	52.8	55.3	50.1	14.40	0.03
Ce	183	326	259	286	127	178	149	118	95	100	95	36.80	0.05
Pr	18.5	37.4	31.4	34.8	11.9	16.6	13.6	11.8	8.92	9.39	9.00	4.94	0.01
Nd	63.3	142	123	132	37.8	52.9	42.6	40.2	29.6	31.0	29.7	24.22	0.03
Sm	9.42	21.9	19.5	20.4	5.30	7.21	5.72	6.15	4.57	4.65	4.71	5.99	0.02
Eu	1.94	4.70	4.41	4.57	1.26	1.60	1.25	1.49	1.07	1.14	1.14	2.01	0.00
Tb	0.857	1.64	1.41	1.45	0.455	0.584	0.445	0.540	0.450	0.430	0.454	0.87	0.00
Gd	6.80	14.18	12.37	12.83	3.50	4.58	3.55	4.18	3.29	3.31	3.41	6.21	0.01
Dy	4.45	7.50	6.32	6.48	2.24	2.86	2.21	2.75	2.36	2.27	2.29	5.21	0.01
Ho	0.815	1.25	1.03	1.07	0.406	0.523	0.402	0.501	0.435	0.415	0.399	0.91	0.00
Er	2.21	3.23	2.55	2.65	1.14	1.47	1.15	1.35	1.22	1.18	1.11	2.51	0.01
Yb	2.02	2.53	1.90	1.96	1.12	1.44	1.18	1.27	1.20	1.16	1.04	1.93	0.01
Lu	0.310	0.354	0.263	0.276	0.164	0.219	0.181	0.185	0.184	0.171	0.150	0.25	0.00
Hf	8.88	4.70	5.24	5.71	4.81	4.73	4.54	4.17	3.94	4.28	3.66	4.31	0.03
Ta	3.27	1.34	1.77	1.37	2.80	3.67	2.67	3.35	3.18	3.50	2.97	1.00	0.00
Pb	16.8	24.7	15.8	20.9	25.7	23.7	27.7	24.6	32.4	25.2	39.2	1.39	0.07
Th	25.4	14.8	14.4	30.3	25.4	38.9	32.2	20.6	18.6	18.2	20.3	1.06	0.01
U	5.00	4.77	3.57	8.49	3.27	5.47	2.47	4.19	2.23	2.13	2.07	0.35	0.01
∑REE	399	721	583	634	266	371	307	253	201	210	198		
(La/Yb)N	45.45	53.43	32.40	46.49	13.68	62.26	40.58	31.24	28.22	31.40	29.25		
Eu/Eu*	0.74	0.82	0.87	0.86	0.89	0.85	0.85	0.90	0.84	0.89	0.87		
Ba/La	6.13	10.78	10.28	16.10	14.97	10.00	10.96	17.49	15.01	13.48	19.36		
Nb/La	0.56	0.20	0.25	0.23	0.55	0.56	0.45	0.62	0.61	0.64	0.58		
Ba/Zr	1.67	8.28	6.54	9.22	4.91	4.50	4.40	6.33	5.11	4.08	6.43		
Rb/Sr	0.25	0.18	0.06	0.10	0.20	0.19	0.19	0.14	0.49	0.31	0.44		
Nb/Ce	0.32	0.10	0.12	0.10	0.32	0.32	0.26	0.34	0.34	0.36	0.31		
Th/Ta	7.77	11.03	8.13	22.09	9.07	10.61	12.04	6.14	5.85	5.18	6.83		

Table 3 LA-ICP-MS U-Pb data on zircons and ages of the MMEs in Mashhad granodiorite

Analysis	Pb ppm	Th ppm	U ppm	Th/U	$^{207}Pb/^{235}U$	$^{207}Pb/^{235}U$ 2 δ error	$^{206}Pb/^{238}U$	$^{206}Pb/^{238}U$ 2 δ error	Rho	$^{206}Pb/^{238}U$ Age (Ma)	$^{206}Pb/^{238}U$ 2 δ error
GE1 (Mean age = 205±1.3 Ma)											
A02	40	699	1034	0.68	0.2249	0.0088	0.03266	0.00114	0.89	207.2	7.1
A04	12	38	383	0.10	0.2285	0.0110	0.03248	0.00114	0.73	206.0	7.1
A08	15	167	419	0.40	0.2297	0.0133	0.03258	0.00117	0.62	206.6	7.3
A09	15	30	517	0.06	0.2271	0.0099	0.03235	0.00111	0.79	205.2	7.0
B01-1	20	12	676	0.02	0.2223	0.0095	0.03226	0.00108	0.79	204.7	6.8
B01-2	15	18	493	0.04	0.2204	0.0097	0.03240	0.00111	0.78	205.6	6.8
B02	14	14	458	0.03	0.2263	0.0099	0.03260	0.00111	0.78	206.8	6.9
B03	42	1012	957	1.06	0.2302	0.0089	0.03254	0.00108	0.86	206.4	6.8
B06-1	58	1138	1452	0.78	0.2249	0.0084	0.03267	0.00108	0.89	207.3	6.8
B06-2	76	2934	1273	2.30	0.2306	0.0095	0.03254	0.00108	0.81	206.5	6.8
B07	49	1014	1244	0.81	0.2244	0.0085	0.03195	0.00105	0.87	202.8	6.6
B09	19	97	589	0.16	0.2598	0.0126	0.03235	0.00108	0.69	205.2	6.8
B10	37	1096	757	1.45	0.2244	0.0090	0.03206	0.00105	0.81	203.4	6.5
C10	19	23	641	0.04	0.2352	0.0107	0.03215	0.00105	0.72	204.0	6.5
D01-1	55	1484	1233	1.20	0.2234	0.0084	0.03218	0.00102	0.84	204.2	6.4
D01-2	52	1577	1097	1.44	0.2387	0.0096	0.03239	0.00105	0.80	205.5	6.5
D03	37	286	1123	0.25	0.2225	0.0085	0.03231	0.00102	0.83	205.0	6.4
D04-1	21	86	689	0.13	0.2221	0.0092	0.03208	0.00102	0.77	203.5	6.4
D04-2	50	241	1575	0.15	0.2235	0.0081	0.03229	0.00102	0.87	204.9	6.3
D06-1	21	118	652	0.18	0.2238	0.0090	0.03232	0.00102	0.78	205.1	6.3
D06-2	21	128	688	0.19	0.2235	0.0089	0.03217	0.00099	0.77	204.1	6.3
D07	42	961	1035	0.93	0.2386	0.0090	0.03218	0.00099	0.81	204.2	6.2
D09	14	25	451	0.06	0.2295	0.0104	0.03253	0.00102	0.69	206.4	6.3
E03	18	107	594	0.18	0.2285	0.0098	0.03213	0.00099	0.72	203.9	6.1
E06	30	59	894	0.07	0.3444	0.0143	0.03311	0.00099	0.72	210.0	6.2
E07	15	49	474	0.10	0.2283	0.0101	0.03249	0.00096	0.67	206.1	6.1
E08-1	15	127	453	0.28	0.2255	0.0112	0.03217	0.00096	0.60	204.1	6.1
E08-2	43	281	1309	0.21	0.2355	0.0084	0.03241	0.00096	0.83	205.6	5.9
E09-1	36	186	1104	0.17	0.2737	0.0101	0.03256	0.00096	0.80	206.6	6.0
E11-1	78	2948	1370	2.15	0.2257	0.0081	0.03237	0.00093	0.80	205.4	5.9

Table 4 Results of whole rock Sr-Nd isotope ratios for the Mashhad granodiorite and their MMEs

Sample No.	Rock types	Sample age (y)	$^{87}Rb/^{86}Sr$	$^{87}Sr/^{86}Sr$	2 StdErr (Abs)	$^{147}Sm/^{144}Nd$	$^{143}Nd/^{144}Nd$	$(^{87}Sr/^{86}Sr)_i$	$(^{143}Nd/^{144}Nd)T$	εNd(t)
B1	Granodiorite	2.05E+08	0.579	0.707475	4.3E-06	0.085	0.512372	0.705788	0.512258	-2.3
G3		2.05E+08	0.554	0.707546	5.2E-06	0.081	0.512356	0.705931	0.512247	-2.5
KE16H		2.05E+08	0.330	0.706869	5.7E-06	0.092	0.512377	0.705906	0.512254	-2.3
R2		2.05E+08	1.427	0.709978	7.1E-06	0.093	0.512345	0.705817	0.512220	-3.0
GE1	MMEs	2.05E+08	0.633	0.707594	5.3E-06	0.089	0.512405	0.705749	0.512285	-1.7
KE16E		2.05E+08	0.174	0.706355	6.0E-06	0.096	0.512432	0.705849	0.512303	-1.4
KE25		2.05E+08	0.718	0.708278	6.5E-06	0.090	0.512385	0.706184	0.512265	-2.1
RE1		2.05E+08	1.216	0.709640	5.1E-06	0.095	0.512397	0.706095	0.512269	-2.1

Highlights:

- Mafic microgranular enclaves (MMEs) are commonly present in Mashhad granodiorite, Northeastern Iran
- The mafic and felsic magmas are derived from partial melting of an enriched lithospheric mantle metasomatized by slab fluid
- The Mashhad granodiorite and its MMEs are the result of the mixing between mafic and felsic magmas